

# Modelling the AGN broad line region using single-epoch spectra – I. The test case of Arp 151

S. I. Raimundo <sup>1</sup>★, A. Pancoast,<sup>2</sup> M. Vestergaard,<sup>1,3</sup> M. R. Goad<sup>4</sup> and A. J. Barth <sup>5</sup>

<sup>1</sup>*DARK, Niels Bohr Institute, University of Copenhagen, Lyngbyvej 2, DK-2100 Copenhagen, Denmark*

<sup>2</sup>*Harvard-Smithsonian Center for Astrophysics, 60 Garden Street, Cambridge, MA 02138, USA*

<sup>3</sup>*Steward Observatory, University of Arizona, 933 N. Cherry Avenue, Tucson, AZ 85721, USA*

<sup>4</sup>*Department of Physics and Astronomy, University of Leicester, University Road, Leicester LE1 7RH, UK*

<sup>5</sup>*Department of Physics and Astronomy, 4129 Frederick Reines Hall, University of California, Irvine, CA 92697-4575, USA*

Accepted 2019 August 7. Received 2019 July 31; in original form 2018 October 17

## ABSTRACT

We show that individual (single-epoch) spectra of active galactic nuclei (AGNs) can constrain some of the geometry and dynamics of the AGN broad line region. Studies of the cosmic influence of supermassive black holes are limited by the current large uncertainties in the determination of black hole masses. One dominant limitation is the unknown geometry, dynamics, and line-of-sight inclination of the broad line region, used to probe the central black hole mass. Recent progress has been made to constrain the spatial and kinematic structure of the broad line region using dynamical modelling of AGN monitoring data and an underlying physical model for the broad line region. In this work we test the ability of a modified version of this dynamical modelling code to constrain the broad line region structure using single-epoch spectra. We test our modelling code on single-epoch spectra of nearby Arp 151 by comparing our results with those obtained with monitoring data of this same object. We find that a significant fraction of the broad line region parameters can indeed be adequately constrained, with uncertainties that are comparable to, or at most a factor of approximately a few higher than those obtained from modelling of monitoring data. Considering the wealth of available single-epoch spectroscopic observations, this method is promising for establishing the overall AGN population trends in the geometry and dynamics of the broad line region. This method can be applied to spectra of AGNs at low and high redshift making it valuable for studies of cosmological black hole and AGN evolution.

**Key words:** galaxies: active – galaxies: individual: Arp 151 – galaxies: nuclei – galaxies: Seyfert.

## 1 INTRODUCTION

Our current theoretical model for active galactic nuclei (AGNs) associates the energy emitted by these objects with mass accretion on to a supermassive black hole (Lynden-Bell 1969). The black hole mass is an essential parameter to understand the growth of black holes and their impact on the surrounding medium. A black hole mass measurement provides a snapshot of the mass growth stage of the black hole, allowing us to probe and constrain the evolution of black holes and their host galaxies (e.g. Shankar et al. 2004; Vestergaard 2004; Raimundo & Fabian 2009). The maximum energy output of the AGN and its physical scale are also set by the mass of the black hole (see Fabian 2012 for a review), providing a reference scale for the possible impact of AGN feedback on the host galaxy.

Black hole masses can rarely be measured directly. We often rely on indirect measurements, such as black hole and AGN scaling relationships, to determine the black hole mass (e.g. Vestergaard 2002; Vestergaard & Peterson 2006; Kormendy & Ho 2013; Peterson 2014). However, there are some objects for which the black hole mass can be determined directly and that are used to define and calibrate the scaling relations. In the local Universe the black hole mass can be determined directly by the measurement of stellar or gas dynamics affected by the black hole’s gravitational potential (e.g. Kormendy & Ho 2013). These methods require nearby targets for which the achievable spatial resolution approaches the small scales where the gravitational potential of the black hole dominates. For black holes that are actively accreting, i.e. AGNs, the black hole mass can be determined via reverberation mapping studies (Blandford & McKee 1982; Peterson 1993; Peterson 2014). In the case of reverberation mapping the limitations are not associated with the resolvable spatial scales. They are instead associated with the required time cadence and long duration of the observations.

\* E-mail: [sandra.raimundo@nbi.ku.dk](mailto:sandra.raimundo@nbi.ku.dk)

Until the quality of monitoring data are sufficient to provide high-fidelity velocity-delay maps, there is also a need to assume a black hole mass scaling relation to account for the unknown broad line region (BLR) structure and kinematics.

In addition to the observational limitations outlined above, reverberation mapping studies require some prior knowledge or physical assumptions on the gas distribution in the vicinity of the black hole. Reverberation mapping relies on the monitoring of the broad emission lines observed in some AGNs. These broad emission lines have velocities  $v_{\text{FWHM}} > 1500\text{--}2000 \text{ km s}^{-1}$  and are emitted by rapidly orbiting gas in the vicinity of the black hole, in the so-called BLR (e.g. Peterson & Wandel 2000). This gas is ionized by continuum photons from the accretion disc, originally produced during the process of gas accretion on to the supermassive black hole. Due to the very small distance between the BLR and the black hole (typically a few light-days to a few light-months for the most luminous AGN), this gas is a probe of the black hole dominated gravitational potential, and hence of the black hole mass. Converting the observed properties of the broad emission lines into a black hole mass estimate depends on the assumed gas distribution within the BLR and its inclination with respect to our line of sight (e.g. Peterson 2014). However, the properties of the gas within the BLR are not well constrained (e.g. Collin et al. 2006) and it is not clear what is the intrinsic geometric structure of the BLR of each AGN.

There is some indication that the broad emission line profile contains information on the distribution of gas velocities in the BLR, where it was produced. This has been suggested based on observed correlations between line properties and AGN inclination (inferred from radio jets) (e.g. Wills & Browne 1986; Vestergaard, Wilkes & Barthel 2000), and from the modelling of single-epoch broad line profiles (e.g. Capriotti, Foltz & Byard 1980; Kwan & Carroll 1982; Eracleous & Halpern 1994; Rosenblatt et al. 1994; Kollatschny & Zetzl 2013; Storchi-Bergmann et al. 2017). However, a single spectrum will only show a snapshot of the integrated emission and gas velocity distribution across the entire BLR.

Most progress in this area has been achieved through multi-epoch spectroscopy as used in reverberation mapping studies, to monitor the time-dependent changes in the line profile. Due to the time delayed response of the BLR with respect to (accretion disc) continuum variations, reverberation mapping campaigns can follow a variation (e.g. a strong increase) in the accretion disc emission as it propagates in time and energy through the BLR. The effect of the ionizing photons as they reach gas in the BLR can be traced in the spectra: each portion of the BLR responds according to its distance to the ionizing continuum, its structure, and its physical conditions as well as its dynamics (Peterson 1997). This will be imprinted on the spectral profiles of the broad lines as the gas in the BLR responds to the continuum variations. The dynamics in particular will be probed via the velocity broadening and velocity changes to the line profiles. Measuring the delayed response of different portions of the BLR provides a method to infer the structure of the BLR, by using time-resolved information as opposed to spatially resolved information.

Reverberation mapping studies have indeed been successful at determining the characteristic size of the BLR, i.e. the responsivity-weighted distance (e.g. Peterson 1993). More recently, the first velocity delay maps that describe how the gas velocities change with time delay during the monitoring campaigns were obtained from reverberation mapping techniques. By comparing the measured time lag as a function of velocity across the broad line with simple models for the kinematic state of the BLR it has been possible to identify

that the BLR in nearby AGNs spans a range of dynamics, including virialized orbital motion, inflows, and outflows (Bentz et al. 2009; Bentz et al. 2010; Denney et al. 2010; Grier et al. 2013; Pei et al. 2017; Xiao et al. 2018).

Additional progress has been achieved by direct modelling of the monitoring data using a geometrical and dynamical model such as by Brewer et al. (2011), Pancoast, Brewer & Treu (2011), Li et al. (2013), Pancoast, Brewer & Treu (2014a), and Pancoast et al. (2018). This model is able to derive quantitative constraints on the BLR geometry and dynamics parameters by assuming an underlying physical model for the BLR. Until now, 17 distinct low-redshift broad line AGNs have been modelled using this technique (Brewer et al. 2011; Pancoast et al. 2012; Pancoast et al. 2014b; Grier et al. 2017a; Williams et al. 2018). Although the physical parameters determined vary between AGNs, the overall results from these studies seem to indicate that the BLR is a close to face-on thick-disc-like structure with dynamics ranging from gas in bound elliptical orbits to gas in inflowing/outflowing trajectories, depending on the AGN. Until now these models have used high-quality monitoring data (typically from reverberation mapping campaigns) to constrain the BLR geometry and dynamics parameters, which limits the number of AGNs that can be modelled.

Due to the necessary large observing time resources required, reverberation mapping campaigns have only been carried out in a small sub-sample of all known broad line AGNs. There are  $\sim 60$  low-redshift AGNs that have been the target of reverberation mapping campaigns to measure their black hole masses (e.g. Peterson et al. 2004; Bentz et al. 2013; Du et al. 2014; De Rosa et al. 2015, see Bentz & Katz 2015 for an updated list). Recent efforts to extend these studies to higher redshift (e.g. Shen et al. 2016; Grier et al. 2017b; Du et al. 2018) and higher luminosities (e.g. Du et al. 2018; Lira et al. 2018) have increased the sample size to more than 100. However, the feasibility of these studies decreases for high redshift and more luminous AGNs that require observing times that can span years or decades (e.g. Kaspi et al. 2007; Lira et al. 2018). This makes it difficult to extend the BLR dynamical modelling analysis to a large sample of AGNs.

Considering the significant resources required to obtain monitoring data, we have initiated a study to investigate to what extent single spectra (i.e. spectra measured at a single time instant as opposed to multiple epochs) can constrain the structural and dynamical parameters that define the BLR. The goal of this paper is to apply the direct modelling approach described by Pancoast et al. (2014b, 2018) to single-epoch spectra. We apply the model to Arp 151, an AGN that has previously been modelled and studied using multiple sets of monitoring data. By using Arp 151 as a test case and comparing our findings with previous results, we can evaluate how much information can be obtained from a single spectrum alone (i.e. in the absence of timing information). If successful, this can be a powerful method to obtain the properties of the BLR of a much larger population of AGNs than those targeted by reverberation mapping campaigns, as there is a very large database of AGNs with single-epoch spectra available in the literature.

In this paper, we develop a modified version of the model presented by Pancoast et al. (2014a), originally developed for AGN monitoring data. Our goal is to test if single-epoch spectra can constrain the structure of the BLR assuming an underlying physical model and an estimate for the size of the BLR. In Section 2 we give a brief description of past implementations of the model and introduce the key modifications that we carry out. We also describe the data used to constrain and test the model. In Section 3 we apply our modified model to single-epoch spectra of the well-studied AGN

Arp 151. We compare and validate our results against previous modelling of the reverberation mapping dataset on Arp 151. In Section 4 we identify those model parameters that can be usefully constrained and to what degree of uncertainty, using our new model implementation. We also outline and discuss how our new approach can be extended and applied to AGN BLR population studies.

## 2 MODEL AND DATA DESCRIPTION

The broad emission lines observed in AGN spectra are produced when the gas distribution in the BLR reprocesses the incident ionizing radiation. The profile of the line produced will be a function of wavelength, and is affected by the spatial distribution, velocity, and physical conditions of the gas in the BLR at the time of emission. The BLR properties can be parametrized using a model with a set of free parameters to account for the possible variety of BLR gas distributions and kinematics. In this section, we describe the model adopted to parametrize the BLR geometry and dynamics, our approach to test the model, and the observational data used to constrain it.

### 2.1 Model description

We use the broad line region phenomenological modelling code described by Pancoast et al. (2014a, 2018). The model defines the source of ionizing photons and the structure and velocity of the gas in the broad line region via a set of free parameters. The AGN accretion disc is set as the ionizing continuum source and modelled as a point source emitting isotropically. The broad line region gas emission is modelled using a large number of point particles with parametrized spatial and velocity distributions. The global particle distribution is flexible and can be, among others, a sphere, disc, shell, or torus. These particles instantaneously reprocess the incident ionizing continuum to produce line emission. The position and velocity of the particles will affect the time delay between changes in the continuum and later changes in the line emission, and the wavelength of the emitted line flux. The model first generates a continuum light curve based on Gaussian processes so that the ionizing flux is known at arbitrary time instants. For a particular set of geometry and dynamics parameters and light-curve parameters the model generates a representation of the broad line region. Each particle in the broad line region will reprocess the continuum emission according to a characteristic time delay. Therefore, an emission line will be composed of reprocessed radiation that corresponds to different instants of the ionizing continuum light curve. Expected emission line profiles are then generated for that specific BLR representation. The emission line profiles and the continuum light curves generated by the model are then compared with observational data to constrain the model parameters. The parameters are constrained via Bayesian inference using DNest3, a Diffusive Nested Sampling algorithm (Brewer, Pártay & Csányi 2009; Brewer, Pártay & Csányi 2010). DNest3 is a Markov Chain Monte Carlo method based on Nested Sampling, an algorithm for Bayesian computation (Skilling 2006). We use this method to explore the parameter space. It has the particular advantage of being able to efficiently explore complex multidimensional parameter spaces including handling strong correlations between the parameters.

The output of the model will be a multidimensional posterior probability distribution from which we extract the posterior probability distribution for each of the BLR parameters. In past implementations, the observational data consisted of a time series

**Table 1.** List of free parameters in the modelling and their corresponding prior probability.

| Parameter name                     | Prior   |
|------------------------------------|---|
| $\beta$                            | Uniform[0, 2]   |
| $\theta_i$                         | Uniform( $\cos(\theta_i)$ (0, $\pi/2$ ))                        |
| $\theta_o$                         | Uniform[0, $\pi/2$ ]  |
| $M_{\text{BH}}$                    | LogUniform( $2.78 \times 10^4$ , $1.67 \times 10^9 M_{\odot}$ ) |
| $\kappa$                           | Uniform[-0.5, 0.5]  |
| $\gamma$                           | Uniform[1, 5]   |
| $\xi$                              | Uniform[0, 1]   |
| $f_{\text{ellip}}$                 | Uniform[0, 1]   |
| $f_{\text{flow}}$                  | Uniform[0, 1]   |
| $\theta_e$                         | Uniform[0, $\pi/2$ ]  |
| New feature in the modified model: |   |
| $\tau_{\text{mean}}$               | Gaussian( $\mu_{\tau}$ , $\sigma_{\tau}$ ) (d)                  |

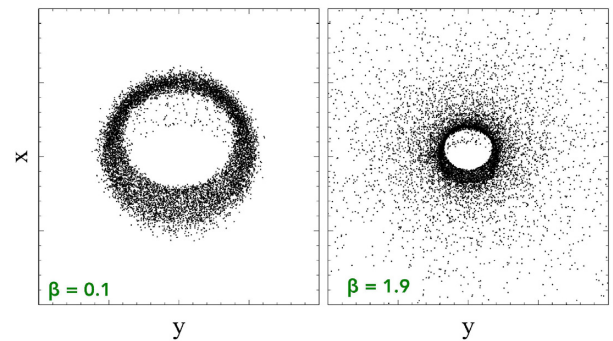


**Figure 1.** Example of a BLR geometry for two different values of  $\beta$ . The black dots represent BLR clouds seen in the  $xy$  plane. The  $\beta$  parameter describes how the clouds are distributed radially, hence  $\beta < 1$  means that the distribution along the radial direction from the centre is Gaussian-like in shape. Left-hand panel:  $\beta = 0.1$ ; right-hand panel:  $\beta = 1.9$ . Both panels assume an inclination angle  $\theta_i = 20^\circ$  and an opening angle  $\theta_o = 30^\circ$ .

of broad emission line profiles and a time series of AGN continuum flux measurements such as those obtained from AGN monitoring campaigns. We describe our modified approach to dealing with single-epoch spectra in Section 2.1.2.

#### 2.1.1 Model parameters

The model uses a set of free parameters with associated prior probability distributions to characterize the geometry and dynamics of the broad line region. Below we give a summary of the parameters and show their assumed prior probability distributions in Table 1. A more in depth parameter description is presented by Pancoast et al. (2014a).

The particle radial distribution is modelled using a Gamma function, with the parameter  $\beta$  controlling the shape of the distribution:  $\beta < 1$  corresponds to a narrow Gaussian-like distribution,  $\beta = 1$  to an exponential profile and  $\beta > 1$  to a profile steeper than an exponential. The Gamma distribution is offset from the origin set by a minimum radius for the BLR. An example of the effect of  $\beta$  in the BLR cloud distribution is shown in Fig. 1. The angular thickness of the BLR, as seen from the black hole, is defined by the opening angle  $\theta_o$ . This angle corresponds to the half angular thickness of the BLR,  $\theta_o = 90^\circ$  for a sphere and approaching  $\theta_o = 0^\circ$  for a thin disc. The BLR is oriented with an inclination angle  $\theta_i$  with respect

to the observer's line of sight:  $\theta_i = 0^\circ$  for a face-on disc and  $\theta_i = 90^\circ$  for an edge-on disc.

There are three parameters that can break the symmetry in the BLR geometry:  $\kappa$ ,  $\gamma$ , and  $\xi$ .

The parameter  $\kappa$  defines if the particles emit isotropically or whether there is preferential emission towards the ionizing source or away from it. For  $\kappa = -0.5$  there is preferential emission towards the ionizing source, for  $\kappa = 0.5$  there is preferential emission away from the ionizing source and for  $\kappa = 0$  the emission is isotropic. Physically it represents an asymmetry in the BLR emission that could be caused by gas within the BLR blocking some of the emission or by an optical depth effect. The parameter  $\gamma$  is used to control the particle displacement angle between the disc plane and the opening angle of the BLR and can have values between 1 and 5. For  $\gamma = 1$  the particles are distributed uniformly and for  $\gamma > 1$  the particles will be more displaced towards the opening angle of the BLR, i.e. more concentrated in the outer face of the BLR disc. Physically,  $\gamma = 5$  may correspond to a situation in which the AGN continuum flux is obscured along the disc mid-plane. The parameter  $\xi$  indicates the transparency of the mid-plane of the BLR. A value of  $\xi = 1$  represents a transparent mid-plane and  $\xi = 0$  an opaque mid-plane.

The black hole mass,  $M_{\text{BH}}$ , sets the gravitational potential of the point particles and no other forces (such as radiation pressure, for example) are considered. The dynamics of the BLR is described by three main parameters that control the type of particle orbit:  $f_{\text{ellip}}$ ,  $f_{\text{flow}}$ , and  $\theta_e$ . Here,  $f_{\text{ellip}}$  constrains the fraction of point particles with near-circular elliptical orbits. The expression  $1 - f_{\text{ellip}}$  corresponds to the fraction of point particles with orbits centred at around the radial inflowing or outflowing escape velocity. The binary parameter  $f_{\text{flow}}$  determines whether a point particle is on an inflowing orbit ( $f_{\text{flow}} < 0.5$ ) centred at the inflowing escape velocity or on an outflowing orbit ( $f_{\text{flow}} \geq 0.5$ ) centred on the outflowing escape velocity. Finally, the inflowing and outflowing velocity distributions can be rotated by  $\theta_e$  towards the circular orbit velocity, so that an increasingly larger fraction of particles are in bound orbits as  $\theta_e \rightarrow 90^\circ$  – see Pancoast et al. (2014a) for further details.

As in Pancoast et al. (2014a) we also do not subtract the narrow emission line component before modelling the data, to avoid introducing uncertainties. The narrow emission line is modelled with a narrow Gaussian function, with the total narrow line flux and systematic central wavelength as free parameters, as described in section 3.3 of Pancoast et al. (2018).

Two additional parameters ( $C_{\text{add}}$  and  $C_{\text{mult}}$ ) are used to normalize the continuum. This makes the modelling independent of the absolute flux level of the continuum and of the emission line. The relevant time-scales are characterized by the mean ( $\tau_{\text{mean}}$ ) and median ( $\tau_{\text{median}}$ ) time lag between the continuum and the line emission. In the original implementation of the model, these two parameters do not have an associated prior probability distribution but are calculated a posteriori from the final BLR geometry and dynamics distribution. We address the time lags differently in this work.

### 2.1.2 Model modifications to analyse single-epoch spectra

The model first described by Pancoast et al. (2011, 2014a) and in its most recent version by Pancoast et al. (2018) was originally built to use multi-epoch monitoring data to constrain the model parameters. That is, the data input for the model is a time series of broad emission line profiles and a time series of AGN continuum

flux measurements. Our goal here is to instead use standard single-epoch spectra as the observational constraint: a spectrum with information on the continuum and the broad line emission measured at a single instant. We modify the model described by Pancoast et al. (2018) to use single-epoch spectra as data input, instead of monitoring data. The main modification we need to make is to add information of the absolute physical scale of the BLR, which we do via a prior probability distribution on the mean time delay between continuum and line emission. Below we describe the modifications implemented on the model.

In the most recent implementation of the model (Pancoast et al. 2018), the physical scale of the BLR was constrained by the temporal (and scale sensitive) information contained in multi-epoch monitoring data. For single-epoch spectra, the temporal information is not available. We must therefore find an alternative method to constrain the physical scale. We do that by setting a prior probability distribution for the mean time delay between the continuum source and the broad line emission, a parameter that in the previous implementation of the model would have been constrained by the temporal information in multi-epoch data. Since the time delay is measured and the light travel speed is known, setting a prior on the mean time delay is equivalent to setting a prior on the size of the broad line region. In practice, we constrain the time delay by adding a Gaussian prior on the mean time delay parameter ( $\tau_{\text{mean}}$ ) in the model. The Gaussian prior centre ( $\mu_\tau$ ) is set at a fixed mean time delay and we define a characteristic width for the Gaussian prior ( $\sigma_\tau$ ) that describes our uncertainty in the prior. The Gaussian prior  $\mu_\tau$  and  $\sigma_\tau$  are free parameters and can be defined (by setting meaningful constraints) for each individual AGN modelled. A prime method to set these constraints is to use the  $R_{\text{BLR}}-L_{\text{AGN}}$  relation (Kaspi et al. 2000; Bentz et al. 2009; Bentz et al. 2013). The  $R_{\text{BLR}}-L_{\text{AGN}}$  relation is a robust observational result that originated from reverberation-mapping studies. It provides an established method to constrain the effective size of the BLR,  $R_{\text{BLR}}$ , from the AGN continuum luminosity,  $L_{\text{AGN}}$ , measured from a single-epoch spectrum. For the single-epoch modelling we carry out in this paper, we always define a Gaussian prior for the time delay. Several options for the choice of the time delay prior parameters will be investigated in this work. In particular, a time delay prior derived from the  $R_{\text{BLR}}-L_{\text{AGN}}$  relation, which is the method of choice for the general AGN population, will be discussed in Section 3.5.

To simulate the variable ionizing continuum light curve we generate a continuous model of the AGN continuum light curve using Gaussian processes, as described by Pancoast et al. (2014a). In past implementations of the BLR model, the AGN continuum model would be determined by interpolating between the points of the observed continuum light curve. In our modified version of the model, we use one continuum flux value and an associated uncertainty estimate as constraint on the continuum light curve. Based on the measured continuum flux and its uncertainty and by extrapolating backwards in time, artificial AGN continuum light curves are generated. These artificial light curves sample a broad range of possible continuum light curves and are formally required for the model to calculate a continuum flux corresponding to the time delay between the continuum emission and each region of the BLR. The range of possible continuum light curves is determined by three main hyper-parameters:  $\mu_{\text{cont}}$ , the long-term mean flux value of the light curve;  $\sigma_{\text{cont}}$ , the long-term standard deviation of the light curve and  $\tau_{\text{cont}}$ , the typical time-scale for variations (see Pancoast et al. 2014a for more details on these parameters). An important point to highlight is that since our single continuum data point does not constrain the continuum light-curve parameters,

our modified version of the code explores the continuum hyper-parameter space to find all the possible realistic solutions during the analysis of the single-epoch spectrum. Since we are not able to constrain the continuum light curve we marginalize the posterior probability distributions over the continuum hyper-parameters. We set flat prior probability distributions for  $\mu_{\text{cont}}$ ,  $\sigma_{\text{cont}}$ , and  $\tau_{\text{cont}}$  and run several tests to determine that the inferred parameters do not depend on the prior range assumed.

## 2.2 Rationale for model verification

After modifying the BLR modelling code to model single-epoch spectra, following the method described in the previous section, our goal is to test the model's performance using real observed spectra. We select the AGN Arp 151 (also known as Mrk 40) for which three reverberation mapping campaigns have already been carried out (Pancoast et al. 2018 and references therein). We extract single-epoch spectra from one of the multi-epoch monitoring datasets (see Section 2.3) and model them individually using our modified version of the model. Each single-epoch spectrum that is modelled results in a predicted set of geometry and dynamics parameters for the BLR.

The full monitoring Arp 151 dataset has been modelled with previous implementations of the model to determine the geometry and dynamics of the BLR (Brewer et al. 2011; Pancoast et al. 2014b; Pancoast et al. 2018). The existence of a monitoring dataset and the associated modelling results are essential in order to evaluate the present model's performance as we can compare the BLR parameters inferred from single-epoch modelling with the BLR parameters obtained from the full monitoring dataset modelling (Pancoast et al. 2014b; Pancoast et al. 2018). This set-up allows us to judge and quantify, in the absence of timing information, the effectiveness of a single spectrum in constraining the parameters of our underlying physical model. In Section 4.2 we discuss in detail the effect of including or not the timing information.

Additionally we validate the model using simulated single epoch spectra. The results of these simulations can be found in Appendix A.

## 2.3 Data

The data we use in this work are part of the Lick AGN Monitoring Project (LAMP) 2008 (Bentz et al. 2009; Walsh et al. 2009) multi-epoch monitoring dataset for Arp 151. LAMP is a long-term project to carry out reverberation-mapping programmes on a selected sample of AGNs. The dataset comprises photometry and spectroscopy monitoring of Arp 151 that covers the spectral region of the broad H $\beta$  emission line ( $\lambda$  [4300 : 7100] Å). The spectra were decomposed into individual contributions from the AGN continuum, host galaxy stellar emission, narrow emission lines, and Fe II emission as described by Barth et al. (2013) and Pancoast et al. (2018).

The advantage of using Arp 151 is that data from the full monitoring campaign are available, which include the continuum light-curve and the H $\beta$  line spectral information. The final decomposed AGN continuum and spectra we use in this work to test the single-epoch BLR modelling approach is similar to the ones used by Pancoast et al. (2018) in their analysis. In this work we will use the multi-epoch monitoring dataset for initial tests and will then extract specific single-epoch spectra for our single-epoch modelling. Our model results will be compared with the ones by Pancoast et al. (2018). Pancoast et al. (2018) test two approaches to modelling the

**Table 2.** Table of inferred parameters for the tests in Fig. 2 using the full light curve. The inferred parameter is the median value of the posterior probability distribution and the uncertainties quoted are the 68 per cent confidence intervals. [1] Parameter name; [2] default simulation by Pancoast et al. (2018): full light curve and no prior; [3] full light curve with a prior on  $\tau_{\text{mean}}$  centred at  $\mu_{\tau} = 3.07$  d and  $\sigma_{\tau} = 0.5\mu_{\tau}$ ; [4] full light curve with a prior on  $\tau_{\text{mean}}$  centred at  $\mu_{\tau} = 3.07$  d and  $\sigma_{\tau} = 3\mu_{\tau}$ ; [5] temperature ( $T$ ) used for each test. More details on  $T$  can be found in Appendix C.

| Parameter                            | No prior                | Prior with<br>$\sigma_{\tau} = 0.5\mu_{\tau}$ | Prior with<br>$\sigma_{\tau} = 3\mu_{\tau}$ |
|--------------------------------------|-------------------------|---|---|
| [1]                                  | [2]                     | [3]   | [4]   |
| $\tau_{\text{mean}}$ (d)             | $3.43^{+0.29}_{-0.32}$  | $3.41^{+0.28}_{-0.27}$                        | $3.45^{+0.30}_{-0.27}$                      |
| $\tau_{\text{median}}$ (d)           | $1.86^{+0.23}_{-0.24}$  | $1.83^{+0.24}_{-0.22}$                        | $1.83^{+0.27}_{-0.25}$                      |
| $\beta$                              | $1.35^{+0.13}_{-0.13}$  | $1.37^{+0.13}_{-0.14}$                        | $1.38^{+0.14}_{-0.16}$                      |
| $\theta_o$ (deg)                     | $26.4^{+3.9}_{-5.9}$    | $27.0^{+5.3}_{-5.3}$                          | $26.9^{+5.9}_{-5.6}$                        |
| $\theta_i$ (deg)                     | $25.8^{+4.2}_{-5.7}$    | $26.4^{+5.0}_{-5.2}$                          | $26.3^{+5.5}_{-5.3}$                        |
| $\kappa$                             | $-0.29^{+0.11}_{-0.10}$ | $-0.32^{+0.09}_{-0.08}$                       | $-0.31^{+0.09}_{-0.09}$                     |
| $\gamma$                             | $3.97^{+0.75}_{-1.10}$  | $4.15^{+0.63}_{-1.07}$                        | $4.11^{+0.64}_{-1.01}$                      |
| $\xi$                                | $0.09^{+0.12}_{-0.06}$  | $0.10^{+0.08}_{-0.06}$                        | $0.09^{+0.08}_{-0.06}$                      |
| $\log_{10}(M_{\text{BH}}/M_{\odot})$ | $6.58^{+0.20}_{-0.12}$  | $6.56^{+0.17}_{-0.13}$                        | $6.58^{+0.16}_{-0.15}$                      |
| $f_{\text{ellip}}$                   | $0.13^{+0.11}_{-0.09}$  | $0.09^{+0.12}_{-0.07}$                        | $0.11^{+0.13}_{-0.08}$                      |
| $f_{\text{flow}}$                    | $0.27^{+0.15}_{-0.18}$  | $0.25^{+0.17}_{-0.17}$                        | $0.25^{+0.18}_{-0.17}$                      |
| $\theta_e$ (deg)                     | $12.7^{+11.3}_{-8.6}$   | $12.0^{+10.3}_{-7.7}$                         | $12.9^{+11.0}_{-9.1}$                       |
| $T$                                  | 65                      | 65  | 80  |

Arp 151 data: fitting the full H $\beta$  line profile and excluding the red wing of the H $\beta$  line profile. Their final inferred BLR parameters quoted in their table 2 are determined from combining the posterior distributions obtained from these two approaches. In this paper we fit the full H $\beta$  emission line profile and will therefore compare our single epoch spectra modelling with the full light-curve modelling of Pancoast et al. (2018) shown as the blue histograms in their fig. 3 (but not quoted in their table 2).

## 3 RESULTS

In this section we describe the tests carried out to evaluate the performance of our single-epoch BLR model. Our goal is to determine how the inferred parameters from single-epoch spectra modelling compare with modelling of the full multi-epoch monitoring dataset. We carried out a set of tests using either the full multi-epoch monitoring dataset or single epoch spectra of Arp 151 extracted from the multi-epoch monitoring. For comparison we use as baseline reference the modelling result of Pancoast et al. (2018), obtained by modelling the LAMP 2008 full multi-epoch monitoring dataset of Arp 151 and the full H $\beta$  line profile described in Section 2.3. From here on, we will refer to their result as the 'full light-curve' modelling. The inferred parameter values for the 'full light-curve' modelling are quoted in the second columns of Tables 2 and 3.

### 3.1 The effect of adding a Gaussian prior on the mean time delay

We first test our main modification to the model, described in Section 2.1.2, which is the addition of a Gaussian prior on the mean time delay ( $\tau_{\text{mean}}$ ). The test is carried out by using our modified version of the model but with the full multi-epoch monitoring dataset as input. This ensures that we isolate the effect of the Gaussian prior on the inferred parameters. As a starting point we

**Table 3.** Table of inferred parameters for the tests we carried out on Arp 151. The inferred parameter is the median value of the posterior probability distribution and the uncertainties quoted are the 68 per cent confidence intervals. [1] Parameter name; [2] default simulation by Pancoast et al. (2018); [3] single epoch (low-flux) with a Gaussian prior on  $\tau_{\text{mean}}$  centred at  $\mu_{\tau} = 3.07$  d and  $\sigma_{\tau} = 0.5\mu_{\tau}$ ; [4] single epoch (mid-flux) with a Gaussian prior on  $\tau_{\text{mean}}$  centred at  $\mu_{\tau} = 3.07$  d and  $\sigma_{\tau} = 0.5\mu_{\tau}$ ; [5] single epoch (high-flux) with a Gaussian prior on  $\tau_{\text{mean}}$  centred at  $\mu_{\tau} = 3.07$  d and  $\sigma_{\tau} = 0.5\mu_{\tau}$ ; [6] single epoch (mid-flux) with a Gaussian prior on  $\tau_{\text{median}}$  centred at  $\mu_{\tau} = 1.75$  d and  $\sigma_{\tau} = 0.5\mu_{\tau}$ ; [7] single epoch (mid-flux) with a Gaussian prior on  $\tau_{\text{median}}$  centred at  $\mu_{\tau} = 3.07$  d and  $\sigma_{\tau} = 0.5\mu_{\tau}$ ; [8] single epoch (mid-flux) with a Gaussian prior on  $\tau_{\text{median}}$  centred at  $\mu_{\tau} = 5.21$  and  $\sigma_{\tau} = 0.2$  dex from the  $R-L$  relation; [9] single epoch (mid-flux) with  $\mu_{\tau} = 15.63$  ( $3 \times R-L$  predicted value) and  $\sigma_{\tau} = 1.2$  dex; [10] single epoch (mid-flux) with  $\mu_{\tau} = 15.63$  ( $3 \times R-L$  predicted value) and  $\sigma_{\tau} = 1.2$  dex. The last row shows the temperature ( $T$ ) used for each test. More details can be found in Appendix C. The parameters are all measured in the rest frame.

| Parameter<br>[1]                     | Single epochs           |                        |                         | $\tau_{\text{median}}$<br>[6] | Mid-flux epoch          |                                      |                                      | (R-L)                            |  |  |
|--------------------------------------|-------------------------|------------------------|-------------------------|-------------------------------|-------------------------|--------------------------------------|--------------------------------------|----------------------------------|--|--|
|                                      | Full light<br>[2]       | Low flux<br>[3]        | Mid flux<br>[4]         |                               | High flux<br>[5]        | $\sigma_{\tau} = 1\mu_{\tau}$<br>[7] | $\sigma_{\tau} = 2\mu_{\tau}$<br>[8] | $\sigma_{\tau} = 0.2$ dex<br>[9] | $3\mu_{\tau}\sigma_{\tau} = 0.2$ dex<br>[10] | $3\mu_{\tau}\sigma_{\tau} = 1.2$ dex<br>[11] |
| $\tau_{\text{mean}}$ (d)             | $3.43^{+0.29}_{-0.32}$  | $3.01^{+1.47}_{-1.56}$ | $3.21^{+1.54}_{-1.72}$  | $3.61^{+1.61}_{-1.73}$        | $3.98^{+3.10}_{-2.49}$  | $6.42^{+3.04}_{-4.23}$               | $5.72^{+2.52}_{-2.29}$               | $9.33^{+1.55}_{-1.76}$           | $3.22^{+5.53}_{-2.60}$                       |  |
| $\tau_{\text{median}}$ (d)           | $1.86^{+0.23}_{-0.24}$  | $1.21^{+0.60}_{-0.64}$ | $1.60^{+0.96}_{-0.85}$  | $1.48^{+0.86}_{-0.64}$        | $2.07^{+1.74}_{-1.32}$  | $3.58^{+2.10}_{-2.51}$               | $3.08^{+1.62}_{-1.37}$               | $5.50^{+1.63}_{-1.31}$           | $1.84^{+3.15}_{-1.51}$                       |  |
| $\beta$                              | $1.35^{+0.13}_{-0.13}$  | $1.75^{+0.15}_{-0.19}$ | $1.46^{+0.22}_{-0.22}$  | $1.53^{+0.12}_{-0.13}$        | $1.49^{+0.21}_{-0.26}$  | $1.51^{+0.25}_{-0.26}$               | $1.54^{+0.22}_{-0.24}$               | $1.61^{+0.19}_{-0.24}$           | $1.49^{+0.27}_{-0.22}$                       |  |
| $\theta_0$ (deg)                     | $26.4^{+3.9}_{-5.9}$    | $9.3^{+19.6}_{-3.9}$   | $22.5^{+12.5}_{-10.7}$  | $12.5^{+12.3}_{-7.4}$         | $23.4^{+11.9}_{-11.3}$  | $21.5^{+10.2}_{-9.3}$                | $20.6^{+11.4}_{-9.6}$                | $18.3^{+11.6}_{-9.2}$            | $20.6^{+9.7}_{-10.3}$                        |  |
| $\theta_1$ (deg)                     | $25.8^{+4.2}_{-5.7}$    | $9.6^{+22.2}_{-3.7}$   | $22.5^{+10.6}_{-9.8}$   | $16.5^{+14.2}_{-7.8}$         | $18.9^{+12.8}_{-7.7}$   | $19.8^{+9.8}_{-6.2}$                 | $21.0^{+10.1}_{-8.7}$                | $17.4^{+9.3}_{-7.3}$             | $20.3^{+8.4}_{-9.0}$                         |  |
| $\kappa$                             | $-0.29^{+0.11}_{-0.10}$ | $0.10^{+0.26}_{-0.37}$ | $-0.18^{+0.23}_{-0.19}$ | $0.14^{+0.26}_{-0.34}$        | $-0.13^{+0.25}_{-0.20}$ | $-0.20^{+0.20}_{-0.18}$              | $-0.16^{+0.26}_{-0.19}$              | $-0.25^{+0.26}_{-0.16}$          | $-0.17^{+0.25}_{-0.19}$                      |  |
| $\gamma$                             | $3.97^{+0.75}_{-1.10}$  | $3.06^{+1.26}_{-1.44}$ | $3.16^{+1.25}_{-1.38}$  | $2.32^{+1.54}_{-0.90}$        | $2.85^{+1.44}_{-1.22}$  | $2.82^{+1.37}_{-1.24}$               | $3.19^{+1.18}_{-1.45}$               | $3.04^{+1.37}_{-1.41}$           | $2.92^{+1.37}_{-1.33}$                       |  |
| $\xi$                                | $0.09^{+0.12}_{-0.06}$  | $0.19^{+0.51}_{-0.14}$ | $0.15^{+0.17}_{-0.09}$  | $0.17^{+0.34}_{-0.13}$        | $0.16^{+0.17}_{-0.11}$  | $0.14^{+0.12}_{-0.08}$               | $0.14^{+0.15}_{-0.09}$               | $0.15^{+0.19}_{-0.10}$           | $0.15^{+0.17}_{-0.10}$                       |  |
| $\log_{10}(M_{\text{BH}}/M_{\odot})$ | $6.58^{+0.20}_{-0.12}$  | $7.20^{+0.56}_{-0.76}$ | $6.72^{+0.48}_{-0.42}$  | $6.89^{+0.51}_{-0.57}$        | $6.91^{+0.41}_{-0.41}$  | $7.11^{+0.41}_{-0.72}$               | $7.09^{+0.47}_{-0.39}$               | $7.43^{+0.51}_{-0.31}$           | $6.91^{+0.55}_{-0.86}$                       |  |
| $f_{\text{chp}}$                     | $0.15^{+0.11}_{-0.09}$  | $0.40^{+0.37}_{-0.23}$ | $0.17^{+0.16}_{-0.11}$  | $0.35^{+0.20}_{-0.19}$        | $0.22^{+0.18}_{-0.15}$  | $0.21^{+0.16}_{-0.16}$               | $0.22^{+0.19}_{-0.14}$               | $0.20^{+0.20}_{-0.12}$           | $0.22^{+0.18}_{-0.14}$                       |  |
| $f_{\text{flow}}$                    | $0.27^{+0.15}_{-0.18}$  | $0.31^{+0.25}_{-0.20}$ | $0.26^{+0.17}_{-0.17}$  | $0.28^{+0.18}_{-0.20}$        | $0.27^{+0.16}_{-0.17}$  | $0.24^{+0.18}_{-0.18}$               | $0.26^{+0.18}_{-0.18}$               | $0.25^{+0.18}_{-0.17}$           | $0.27^{+0.17}_{-0.18}$                       |  |
| $\theta_e$ (deg)                     | $12.7^{+11.3}_{-8.6}$   | $27.3^{+43.2}_{-18.9}$ | $12.3^{+12.1}_{-8.3}$   | $17.9^{+27.8}_{-12.4}$        | $12.0^{+14.7}_{-8.0}$   | $12.6^{+11.5}_{-8.9}$                | $13.7^{+14.5}_{-9.4}$                | $11.4^{+14.3}_{-7.5}$            | $12.2^{+15.0}_{-8.7}$                        |  |
| $T$                                  | 65                      | 1                      | 1                       | 1                             | 3                       | 1                                    | 3                                    | 3                                | 3  |  |

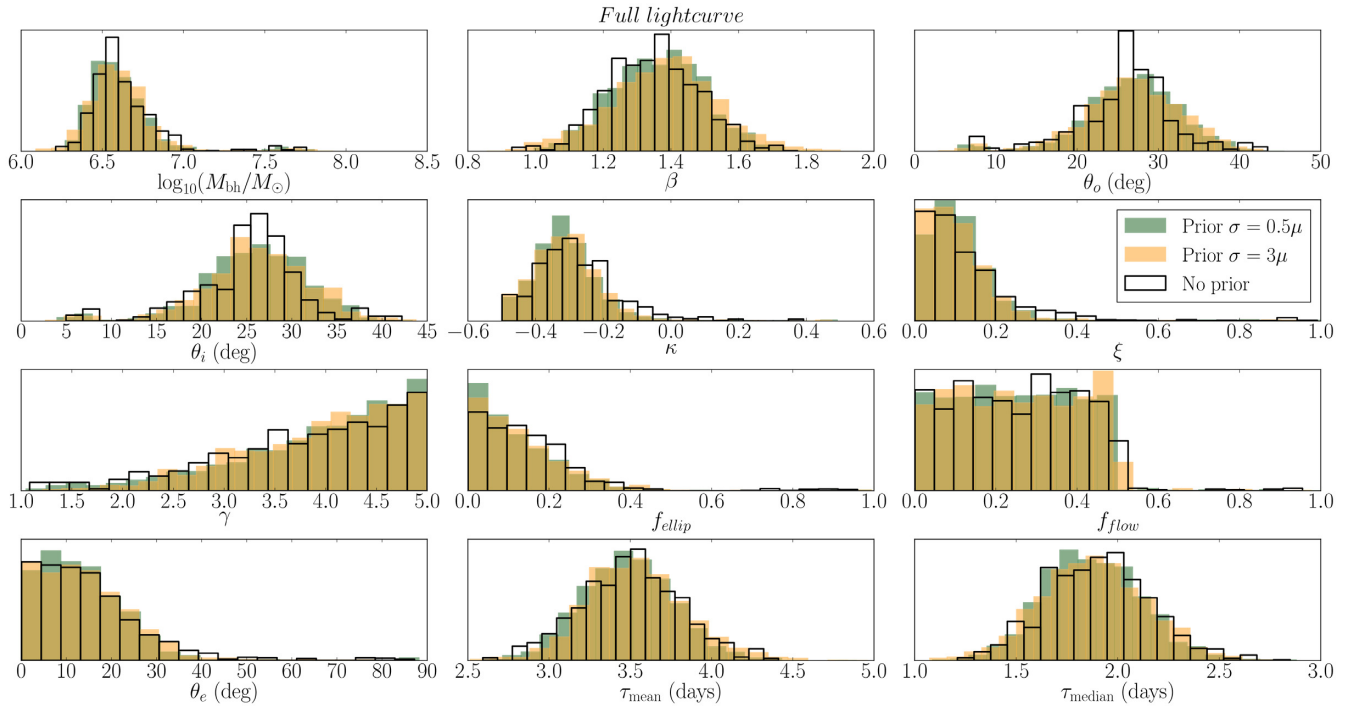


**Figure 2.** Posterior probability distributions for the geometry and dynamics parameters of the BLR of Arp 151 when modelling the full spectroscopic and photometric light curves. Default modelling of the full light curve without a Gaussian prior (Pancoast et al. 2018) is shown as the black solid line histogram. The filled histograms show the result of using different Gaussian priors on  $\tau_{\text{mean}}$ . In both cases we use a Gaussian distribution centred at  $\mu_{\tau} = 3.07$  d but differ on the width ( $\sigma_{\tau}$ ) of the distribution. The green histogram uses  $\sigma_{\tau} = 0.5 \times \mu_{\tau}$  and the orange histogram  $\sigma_{\tau} = 3 \times \mu_{\tau}$  to represent a well determined value of  $\tau_{\text{mean}}$  and one with higher associated uncertainty. There is no significant difference in the median and 68 per cent confidence range of the posterior distributions between using or not using a Gaussian prior on  $\tau_{\text{mean}}$ .

need to choose the parameters for the  $\tau_{\text{mean}}$  Gaussian prior: the mean  $\mu_{\tau}$  and the standard deviation  $\sigma_{\tau}$ . In practice, the Gaussian prior represents a best measurement of  $\tau_{\text{mean}}$  with an associated measurement uncertainty. For these first tests we decide to match  $\mu_{\tau}$  to the inferred  $\tau_{\text{mean}}$  value based on a previous multi-epoch modelling of Arp 151. At the start of our tests the final results of Pancoast et al. (2018) on Arp 151 were not yet available. We therefore used the inferred  $\tau_{\text{mean}}$  from an earlier model of the Arp 151 LAMP 2008 data (Pancoast et al. 2014b) as our assumed  $\mu_{\tau}$ . Due to the computational time required to run our models, we did not repeat our analysis using the value of  $\tau_{\text{mean}}$  found by Pancoast et al. (2018). However, our assumed confidence ranges in  $\tau_{\text{mean}}$  encompass the Pancoast et al. (2018)  $\tau_{\text{mean}}$  inferred value.

Pancoast et al. (2014b) infer that  $\tau_{\text{mean}} = 3.07^{+0.25}_{-0.2}$  d. We set the  $\tau_{\text{mean}}$  Gaussian prior to be centred at this value:  $\mu_{\tau} = 3.07$ . We set  $\sigma_{\tau}$  to be 0.5 and 3 times the mean time delay ( $\mu_{\tau}$ ) in the prior, i.e. 1.54 and 9.21 d, respectively. These uncertainties correspond to a 68 per cent confidence range of 3.08 and 18.4 d, which are conservatively larger than the inferred  $\tau_{\text{mean}}$  68 per cent confidence range of 0.45 d, determined by Pancoast et al. (2014b). Our approach is equivalent to increasing the uncertainty on the prior value of  $\tau_{\text{mean}}$  so that we do not start with stringent assumptions.

We expect our modified model to give a similar set of inferred parameters as in Pancoast et al. (2018) since for this test we are using exactly the same dataset to constrain the model, the only difference is that in our modified model we use a Gaussian prior on  $\tau_{\text{mean}}$ .

The output of the BLR modelling is the posterior probability distribution function for each of the parameters describing the geometry and dynamics of the BLR. For most of the tests we

show the posterior probability distributions for the parameters obtained from our model. In Fig. 2 we compare the posterior distributions for Arp 151 with and without a prior on  $\tau_{\text{mean}}$ . The results for the full light-curve baseline model from Pancoast et al. (2018) (with no prior on  $\tau_{\text{mean}}$ ), are shown as the solid black line histograms. These histograms correspond to the blue histograms in fig. 3 of Pancoast et al. (2018). The filled histograms show the result of using a prior centred at  $\mu_{\tau} = 3.07$  d with  $\sigma_{\tau} = 0.5 \times \mu_{\tau}$  (green) and a prior centred at  $\mu_{\tau} = 3.07$  d but with a larger uncertainty  $\sigma_{\tau} = 3 \times \mu_{\tau}$  (orange). In Table 2 we show the inferred parameter values for each test. The inferred parameter is the median value of the posterior probability distribution and the uncertainties quoted are the 68 per cent confidence intervals. The diagram and the table show that adding the Gaussian prior with varying widths does not affect the posterior distributions for the parameters. Therefore we can conclude that adding a Gaussian prior on  $\tau_{\text{mean}}$  does not affect significantly the inferred parameter values.

### 3.2 Three single-epoch spectra and the effect of the flux level

In this section we explore modelling the BLR geometry and dynamics of Arp 151 using a single epoch of the light curve (i.e. a spectrum) and show how the results depend on the chosen epoch.

We start by selecting three epochs (i.e. three time instants) in the Arp 151 multi-epoch monitoring light curve. These epochs are representative in terms of the continuum mean flux state of the source and include an epoch at relatively low-flux ‘Low-flux

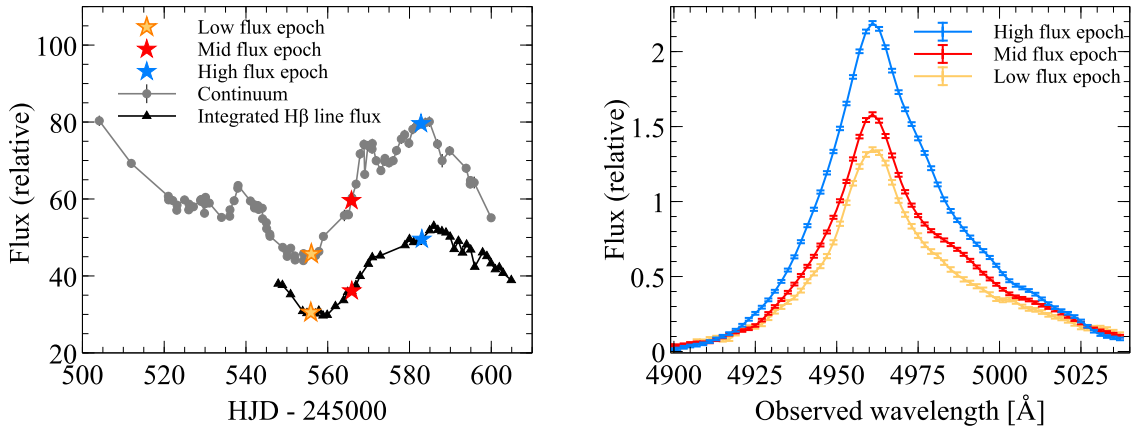


**Figure 3.** Diagrams showing the LAMP 2008 optical light curves of Arp 151 and the epochs chosen for our study. Left: Arp151 continuum light curve (grey circles) and integrated broad  $H\beta$  emission line flux light curve (black triangles). The three single epochs are highlighted by the coloured stars. Right: Spectra covering the broad  $H\beta$  emission line corresponding to each of the epochs selected in the light curve. The line profiles shown were those obtained from spectral decomposition.

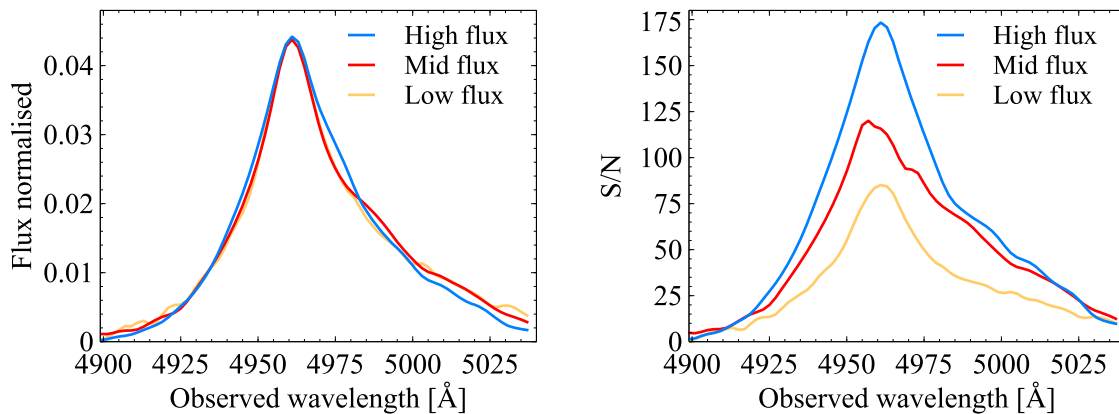


**Figure 4.** Comparison of the continuum-subtracted  $H\beta$  spectral line profiles and the signal-to-noise ratio for the three epochs colour coded as in Fig. 3. Left-hand panel: Line profile shapes normalized to the integrated line flux to ease the comparison between line shapes. Right-hand panel: Signal-to-noise ratio of the continuum subtracted profiles.

epoch’, an epoch at high-flux ‘High-flux epoch’ and an epoch with intermediate flux ‘Mid-flux epoch’, identified from the continuum light curve. In Fig. 3 we show the three selected epochs overlaid on the full continuum light curve and the line integrated flux light curve from the monitoring campaign. The line integrated flux light curve is obtained by integrating the observed spectrum between 4900 and 5050 Å for each individual epoch. On the right-hand panel we show the corresponding spectrally decomposed emission line profile measured at the specific epoch. The spectral profiles are selected from the  $H\beta$  line flux light curve of Fig. 3 (black triangles). For each of the above-mentioned epochs we choose the emission-line epoch that is closest in time to the continuum epoch. In practice, the modified model only needs a continuum value and an associated uncertainty. Using the mean of the two continuum values that encompass the epoch of the line profile measurement does not affect the outcome of our test. This is because the absolute continuum flux value does not affect the outcome of the model, as the continuum flux is normalized. There are two free parameters in the model (a multiplying constant and an additive constant) that re-scale the continuum flux (e.g. Pancoast et al. 2011), as described in Section 2.1.1.

The shape of the line profiles for the three epochs can be more easily compared in Fig. 4. The left-hand panel shows each line profile normalized to its total integrated flux. The right-hand panel shows the signal-to-noise ratio for each epoch.

To set the physical scale we once again implement a Gaussian prior on  $\tau_{\text{mean}}$  centred at the inferred value found by Pancoast et al. (2014b) when modelling the full light curve, i.e. 3.07 d, and an uncertainty of  $\sigma_{\tau} = 1.54$  d. As in the previous section, we deliberately use a conservative width for the Gaussian prior which corresponds to a wider 68 per cent confidence range (3.08 d) than that found by Pancoast et al. (2014b) (0.45 d) for the inferred  $\tau_{\text{mean}}$ . We model each of the three epochs independently, the only common assumption is a similar prior for the mean time delay. We use our continuum model to extrapolate the continuum light curve backwards in time. Since the continuum acts as the ionizing source and it is located at a certain distance from the BLR, we need to simulate a past continuum flux history responsible for producing the broad line emission observed at the present time. This extrapolated continuum light curve does not necessarily reproduce what has been observed in the multi-epoch monitoring campaign. We are simulating a typical situation in AGN studies where we

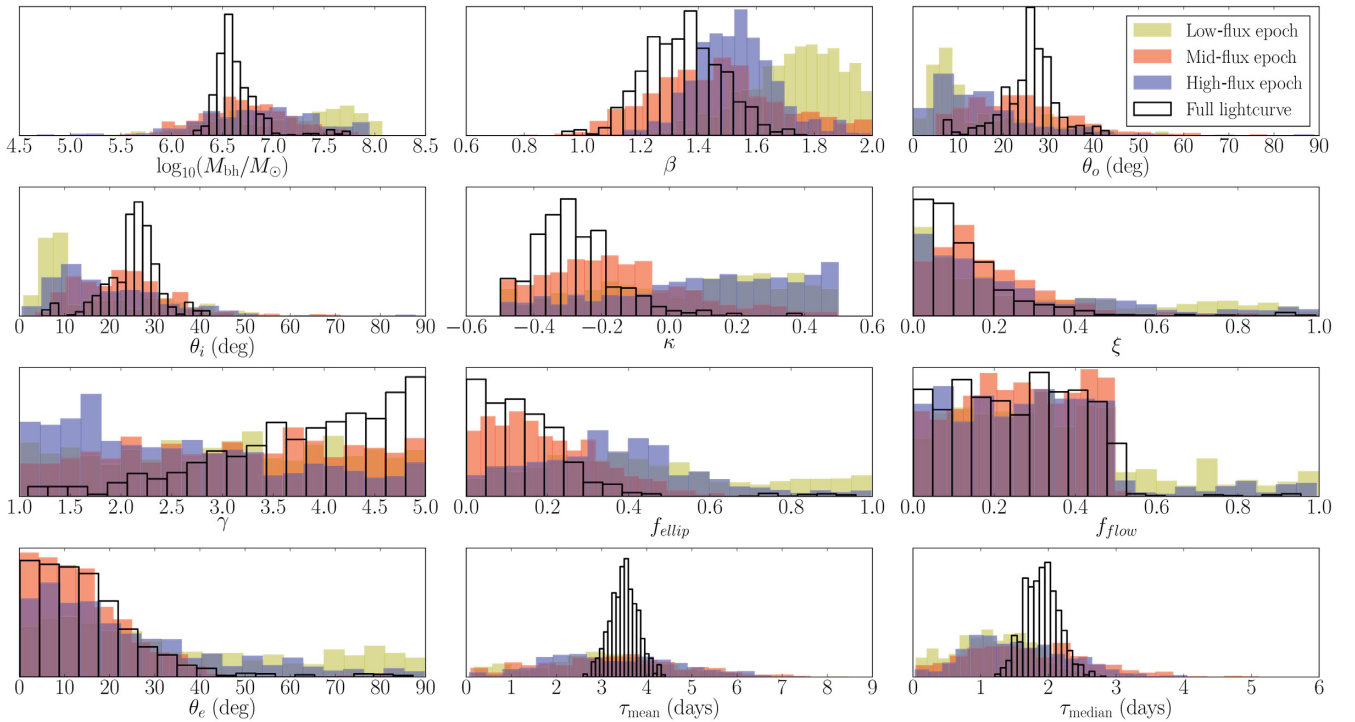


**Figure 5.** Posterior probability distributions for the geometry and dynamics parameters of the BLR of Arp 151 when modelling three single epochs independently. Default modelling of the full light curve without a Gaussian prior (Pancoast et al. 2018) is shown as the black solid line histogram. The filled histograms show the result for each of the epochs as labelled, using a Gaussian prior on  $\tau_{\text{mean}}$  centred at  $\mu_{\tau} = 3.07$  d and with  $\sigma_{\tau} = 0.5\mu_{\tau}$ .

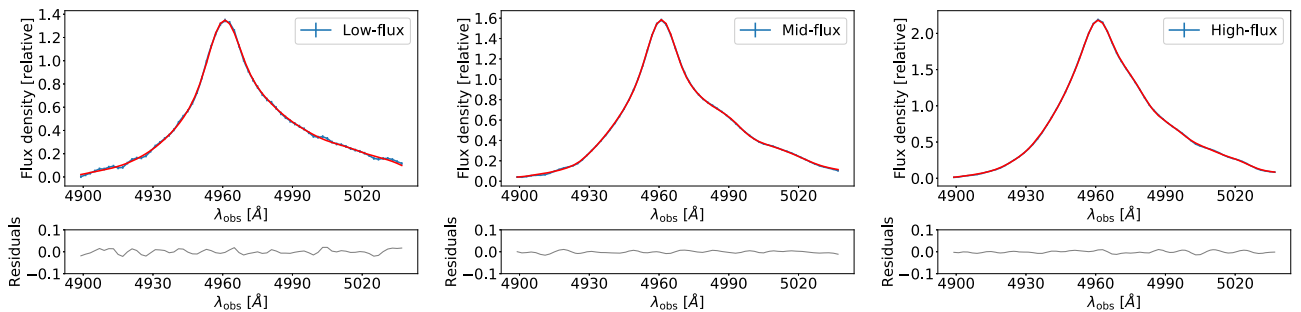


**Figure 6.** Comparison between the input observed spectrum and a representative model line profile drawn from the posterior probability distribution for each epoch. The data are in blue, the model in red, and the residuals are shown in grey in the bottom panels.

only have access to observations at one epoch by performing our analysis based on a wealth of simulated light curves, as explained in Section 2.1.2. A single epoch does not have enough information to determine what is the real continuum light curve for Arp 151. As we will show below, we can still infer some of the BLR parameters even when there is no information on the real continuum light curve.

The results of the modelling for each epoch are shown in Fig. 5. As a comparison, the posterior distribution obtained by Pancoast et al. (2018) with the full light-curve modelling is shown as the black solid line histogram. The posterior distribution for each parameter is consistent within the 68 per cent confidence range among epochs but also broader in general than what was found using the full light curve. This is expected if there is less information in a single epoch spectrum to derive the geometry and dynamics of the BLR. However, the inferred values of the parameters for each of the epochs and the full light curve do agree within the 68 per cent confidence range, which indicates (1) that some of the structural and

dynamical information about the BLR is included in a single epoch; (2) that the BLR geometry and dynamics information is not strongly dependent at which flux level of a light curve a particular epoch was observed. This suggests that provided that a good estimate for the mean time lag is available, some of the geometry parameters can be recovered using single epoch spectra. The inferred parameters and their uncertainties are shown as cases [2], [3], and [4] in Table 3 and in Fig. 7. In Fig. 6 we also show a representative comparison between the model, data, and respective residuals for each epoch. We show the input spectrum in blue and an example of a model line profile drawn from the posterior probability distribution in red. The residuals (data model) are shown in the bottom panel. The model generated profiles shown here are representative of the solutions found in the posterior probability distribution.

The mid-flux epoch appears to be the epoch that more closely approaches the results for the full light curve, possibly because the particular line shape observed at that epoch allows us to decrease the

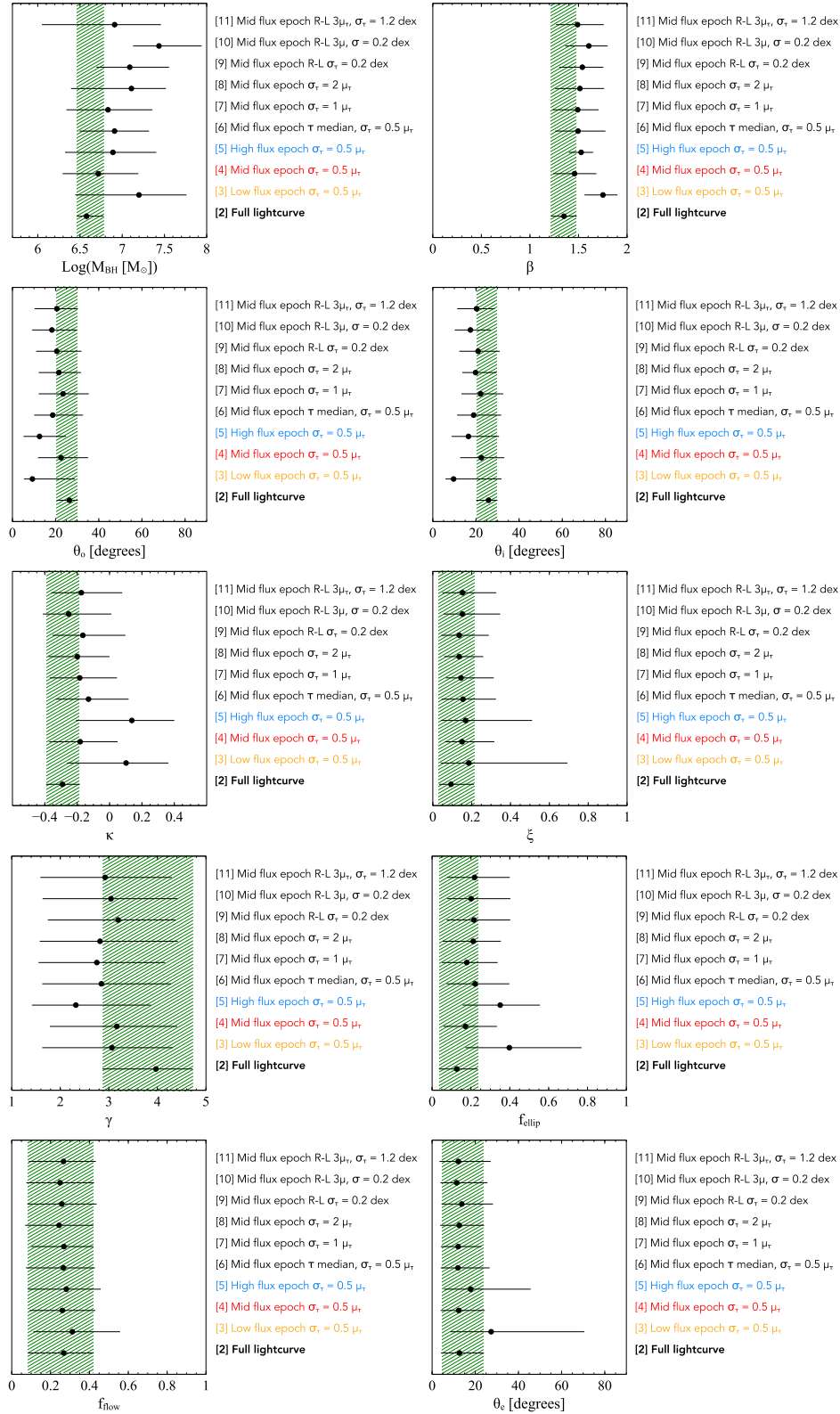


**Figure 7.** Inferred values for the parameters and their respective 68 per cent confidence regions for each of the tests carried out in this work. The shaded green vertical region is the 68 per cent confidence region for the inferred parameters, determined from the full light-curve modelling result in Pancoast et al. (2018). The inferred parameter value is determined from the median of the parameter posterior probability distribution. Scale in the y-axis is arbitrary for drawing purposes. Each test is labelled with a number referring to the relevant column of inferred parameters in Table 3.

uncertainties on the inferred parameters. The low-flux epoch gives the most dissimilar results in terms of constraints on the parameters, in particular predicting higher values for the  $\beta$  parameter, which describes the shape of the spatial distribution of the BLR emission. This is the only parameter for which the inferred value is not within the 68 per cent confidence range of the full light curve inferred  $\beta$ . The low-flux epoch also predicts lower values for the angles than when using the full light curve but with a wide distribution, which makes the inferred values still consistent within the uncertainties. The higher inferred  $\beta$  is not the effect of assuming a prior on the mean time delay because in Fig. 2 this is not observed. It is likely that high- or low-flux states may highlight significantly different portions of the BLR and therefore  $\beta$  will describe the portion of BLR highlighted and not the full BLR distribution. For example, at a specific epoch a different portion of the BLR may be emitting, allowing the model to access information that was not present in the spectra of the other epochs.

### 3.3 Using a prior on $\tau_{\text{mean}}$ or $\tau_{\text{median}}$

Our ultimate goal is to apply the single epoch BLR modelling to other AGNs and therefore in the following tests we will continue to use a single-epoch spectrum for the BLR modelling, as in Section 3.2. We choose the mid-flux epoch of Arp 151 as an example, as its inferred parameters are closest to the full light-curve-inferred parameters.

We test if there is a difference between the modelling results when using a prior on the mean ( $\tau_{\text{mean}}$ ) or median ( $\tau_{\text{median}}$ ) time delay. We find that there is no significant difference between these two approaches, as described next.

Pancoast et al. (2014b) found that, for Arp 151, the mean time delay determined by the model,  $\tau_{\text{mean}}$ , matched the values quoted by Bentz et al. (2009) for the reverberation mapping cross-correlation time lag and therefore should give a better indication of the BLR size. The time lags quoted by Bentz et al. (2009) were used to calculate the BLR radius for the radius–luminosity relation. However, for one of the modelled AGNs by Pancoast et al. (2014b), SBS 1116+583A, the time lag from reverberation mapping is closer to the median time delay ( $\tau_{\text{median}}$ ) obtained from the model. For the purpose of testing if there is a difference in constraining  $\tau_{\text{mean}}$  or  $\tau_{\text{median}}$ , we will now use a Gaussian prior on  $\tau_{\text{median}}$  as opposed to  $\tau_{\text{mean}}$  on single epoch spectra modelling. We use the mid-flux epoch of Arp 151 and set a Gaussian prior on  $\tau_{\text{median}}$ , centred at the inferred value of 1.75 d from BLR modelling of the full light curve (Pancoast et al. 2014b). We assume  $\sigma_{\tau} = 0.5 \times \mu_{\tau}$ , i.e.  $\sigma_{\tau} = 0.875$  d.

We find that the posterior distribution for the parameters is consistent, within the 68 per cent confidence ranges, between all three cases shown. A figure showing the posterior distributions can be found in Fig. B1 in Appendix B. However, a prior on  $\tau_{\text{mean}}$  (red histogram) appears to produce a better match to the full light-curve results for  $M_{\text{BH}}$ ,  $\beta$ ,  $\theta_o$ , and  $\theta_i$  as can be seen from Fig. 7, and Table 3 cases [4] and [6]. Additionally,  $\tau_{\text{mean}}$  appears to be closer to the reverberation mapping time delay measured for most sources (Pancoast et al. 2014b; Grier et al. 2017a). In Fig. 8 we show  $\tau_{\text{mean}}$  and  $\tau_{\text{median}}$  as a function of the cross-correlation time delay for all the sources modelled by Pancoast et al. (2014b) and Grier et al. (2017a). It has been shown that for Arp 151 in particular,  $\tau_{\text{mean}}$  is the best indicator of the cross-correlation time delay. This could be due to the fact that the mean time delay or mean radius is more sensitive to long tails in the particle radial distribution and therefore more sensitive to  $\beta$ . We will therefore continue to use a Gaussian

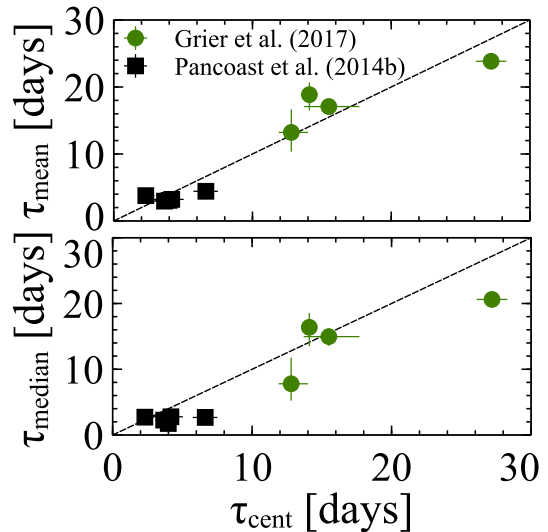


**Figure 8.** Model-determined  $\tau_{\text{mean}}$  (top panel) and  $\tau_{\text{median}}$  (bottom panel) calculated by Pancoast et al. (2014b) (black squares) and Grier et al. (2017a) (green circles) for a sample of AGNs with reverberation mapping data. Mean and median time delays are shown as a function of the reverberation mapping cross correlation time delay  $\tau_{\text{cent}}$  determined by Bentz et al. (2009) and Grier et al. (2012). The dashed line shows the 1:1 relation.

prior on  $\tau_{\text{mean}}$  to explore a possible extension of this study to a more general set of sources.

### 3.4 Changing the mean and confidence range of the Gaussian prior

In this section we are interested in testing what is the effect of increasing the  $\tau_{\text{mean}}$  Gaussian prior distribution width ( $\sigma_{\tau}$ ). This test represents a scenario in which  $\tau_{\text{mean}}$  may not be well known and one wants to increase the uncertainty associated with that measurement.

#### 3.4.1 Width of the Gaussian prior

We use different  $\sigma_{\tau}$  ( $0.5 \times \mu_{\tau}$ ,  $1 \times \mu_{\tau}$ ,  $2 \times \mu_{\tau}$ ) for the Gaussian prior, where  $\mu_{\tau}$  is the Gaussian mean. We set  $\mu_{\tau} = 3.07$  d as in the previous test. We find that with a fixed value for  $\mu_{\tau}$ , the uncertainty associated with the  $\tau_{\text{mean}}$  prior does not significantly impact the inferred parameter values as they are still consistent within the 68 per cent confidence ranges. For  $M_{\text{BH}}$  and the time delays ( $\tau_{\text{mean}}$  and  $\tau_{\text{median}}$ ), the width of the Gaussian prior naturally influences the precision of the inferred values, as the final posterior distributions are wider. For the remaining parameters, the prior width does not seem to have a significant effect, as the mean posterior values and uncertainties appear to be mostly constrained by the input spectrum and not by the width of the prior. This can be more clearly seen from the inferred parameters and associated uncertainties for this test, shown in columns 4, 7, and 8 of Table 3 and in Fig. 7. The posterior probability distributions are shown in Fig. B2 in Appendix B.

#### 3.4.2 Mean value of the Gaussian prior

We also test if changing the mean value of the Gaussian prior ( $\mu_{\tau}$ ) will affect the inferred parameters. We assume a case where  $\mu_{\tau} = 5.21$  d, the value corresponding to the  $R_{\text{BLR}}-L_{\text{AGN}}$  expected value for Arp 151 which is higher than the value of  $\tau_{\text{mean}} = 3.07$  d found by Pancoast et al. (2014b). We assume  $\sigma_{\tau} = 2 \times \mu_{\tau} = 2 \times 3.07$  as

for the test in the previous section. This simulates a situation where the mean value for the Gaussian prior is offset from the real  $\tau_{\text{mean}}$ , but still within the 68 per cent confidence range of the real  $\tau_{\text{mean}}$ . We find that offsetting  $\mu_\tau$  from the real  $\tau_{\text{mean}}$  does not strongly impact the inferred parameters. The posterior probability distributions for this case compared with the full light-curve result and the test in the previous section are shown in Fig. B3 in the Appendix B.

### 3.5 Using the radius–luminosity relation to constrain single-epoch spectra modelling

In this section we extend the scope of our previous tests and describe how to model the BLR of the more general AGN population. In the previous tests we used prior knowledge of the  $\tau_{\text{mean}}$  of Arp 151 to set the physical scale for the model. For the general AGN population such information is not available, however, we will show that the AGN radius–luminosity relation derived for the H  $\beta$  line can be used to set the needed constraints in the model.

As mentioned in Section 2.1.2, the radius–luminosity ( $R_{\text{BLR}}-L_{\text{AGN}}$ ) relation (Kaspi et al. 2000; Bentz et al. 2009; Bentz et al. 2013) establishes a correlation between the characteristic size of the BLR,  $R_{\text{BLR}}$ , and the AGN continuum luminosity,  $L_{\text{AGN}}$ . This relation was determined based on monitoring data in reverberation mapping studies, using the time delay between the AGN continuum and the broad line region response to derive a characteristic size of the BLR. The  $R_{\text{BLR}}-L_{\text{AGN}}$  relation can be used to determine the broad line region size of a much larger sample of AGNs for which meaningful monitoring data have not been, or are difficult to obtain. The community has used this relation to extend BLR size and black hole mass measurements to a wider population of AGNs for which only single-epoch spectra exist (e.g. McLure & Jarvis 2002; Vestergaard 2002; Vestergaard & Peterson 2006; Shen et al. 2011; Kozłowski 2017).

As we showed in our tests, some knowledge of the mean time delay together with BLR modelling can produce meaningful constraints on the BLR geometry and dynamics parameters, even when single epochs are used. Many known AGNs have single epoch measurements that provide spectroscopy covering the H  $\beta$  line and the continuum. The  $R-L$  relation can be used to determine the effective size of the variable BLR (parametrized by  $R_{\text{BLR}}$ ) from the AGN continuum luminosity,  $\lambda L_\lambda$ , (Bentz et al. 2013):

$$\log \left[ \frac{R_{\text{BLR}}}{1 \text{ lt-day}} \right] = 1.527^{+0.031}_{-0.031} + 0.533^{+0.035}_{-0.033} \log \left[ \frac{\lambda L_\lambda}{10^{44} \text{ erg s}^{-1}} \right]. \quad (1)$$

This relation has been derived based on data on the H  $\beta$  broad line emission and has a scatter of typically 0.2 dex Bentz et al. (2013). We should highlight that single-epoch spectra include starlight emission flux from the galaxy. To determine the AGN continuum it is necessary to remove the galaxy starlight contribution via spectral decomposition or, better yet, via surface brightness modelling of images, when available (e.g. Bentz et al. 2013). For more luminous AGNs the galaxy starlight contribution will be less important than for lower luminosity AGNs.

For the purpose of our work, since  $R_{\text{BLR}}$  measured in light-days is a proxy for the mean time delay,  $\tau_{\text{mean}}$ , the  $R-L$  relation can provide the necessary constraints on  $\tau_{\text{mean}}$  based on the AGN continuum luminosity. As we have shown in the previous sections, information on  $\tau_{\text{mean}}$  is the only constraint needed to extend our analysis of the

BLR geometry and dynamical modelling to a large sample of AGNs with single-epoch data.

To test this method, we simulate the conditions that would be available for a typical AGN which is not a multi-epoch monitoring target: a spectrum containing information on the H  $\beta$  line profile, the AGN continuum luminosity at 5100 Å and the  $R-L$  relation. We use a single epoch of Arp 151 as a test since we know the intrinsic BLR parameters from modelling the full light curve. We choose the mid-flux epoch and use the AGN 5100 Å continuum luminosity for Arp 151 measured by Bentz et al. (2013) after accounting for the galaxy’s starlight contribution:  $\lambda L_{\lambda, \text{AGN}} = 3.02 \times 10^{42} \text{ erg s}^{-1}$ . Using this continuum value and the radius–luminosity ( $R-L$ ) relation quoted by Bentz et al. (2013) (equation 1), we obtain an estimated  $R_{\text{BLR}} = 5.21$  light-days. The radius determined is different from the cross-correlation time delay value measured directly by Bentz et al. (2013) (3.99 d) and used to calculate the  $R-L$  relation itself. This is because Arp 151 lies slightly below the  $R-L$  relation. Nevertheless we will set  $\mu_\tau = 5.21$  d since this simulates a situation without prior knowledge on the reverberation mapping results.

Bentz et al. (2013) find a spread of  $\sim 0.2$  dex in the logarithm of  $R_{\text{BLR}}$ . To mimic these findings we set a Gaussian prior in the logarithm of  $\tau_{\text{mean}}$ , centred at  $\mu_\tau = 5.21$  d and with  $\sigma_\tau = 0.2$  dex, and perform the BLR modelling using the Arp 151 mid-flux epoch spectrum. In addition to the default parameters described above, we also test a case where we use a different mean value ( $\mu_\tau$ ) for the Gaussian prior. This is to simulate a situation where the  $R-L$  relation predicts a mean time delay that is too high (in our tests by a factor of 3) compared with the intrinsic unknown value. In the latter test we assume two possible values for  $\sigma_\tau$ , the default of 0.2 dex and a significantly higher uncertainty of 1.2 dex.

The results are shown in Fig. 9. For the case where we use the  $R-L$  relation results directly (blue histogram) the posterior distributions are consistent with the results for the full light curve. This is an important result considering that the  $R-L$  relation itself overestimates  $R_{\text{BLR}}$  for Arp 151. The inferred geometry and dynamics parameters ( $\beta$ ,  $\theta_o$ ,  $\theta_i$ ,  $\kappa$ ,  $\xi$ ,  $\gamma$ ,  $f_{\text{ellip}}$ ,  $f_{\text{flow}}$ , and  $\theta_e$ ) are consistent within the uncertainties with what has been determined from the full light-curve modelling, as can be seen in columns 9, 10, and 11 of Table 3 and in Fig. 7. The black hole mass is more strongly correlated with the time delay. The worst result is obtained when the  $R_{\text{BLR}}$  is overestimated by a factor of  $3 \times$  while maintaining a narrow uncertainty of  $\sigma_\tau = 0.2$  dex on the prior (yellow histogram). This set-up does not allow the model to significantly explore the low black hole mass region which results in an overestimated  $M_{\text{BH}}$ . The last case where  $\sigma_\tau = 1.2$  dex (red histogram) results in a broader posterior distribution and larger final uncertainty in the inferred black hole mass. For this case the broad distribution encompasses the  $M_{\text{BH}}$  estimate based on the full light-curve results.

Our test case of  $\mu_\tau = 3 \times$  the  $R-L$  inferred value is somewhat extreme, considering that the intrinsic dispersion in the  $R-L$  relation is 0.2 dex (Bentz et al. 2013). However our goal was to show the model’s behaviour when tested with extreme cases. Considering this, it is remarkable that the inferred parameters for this test are consistent within the 68 per cent confidence range with the result from the full light curve, as can be seen in Fig. 7. The test we carried out for this extreme case may also be helpful in light of recent findings of samples of AGNs that lie below the  $R-L$  relation (e.g. Grier et al. 2017b; Du et al. 2018).

From these tests we can infer that some of the information on the BLR geometry and dynamics parameters is contained in the spectrum and does not completely depend on the assumed prior on the time delay to set the parameters. We want to highlight that all of

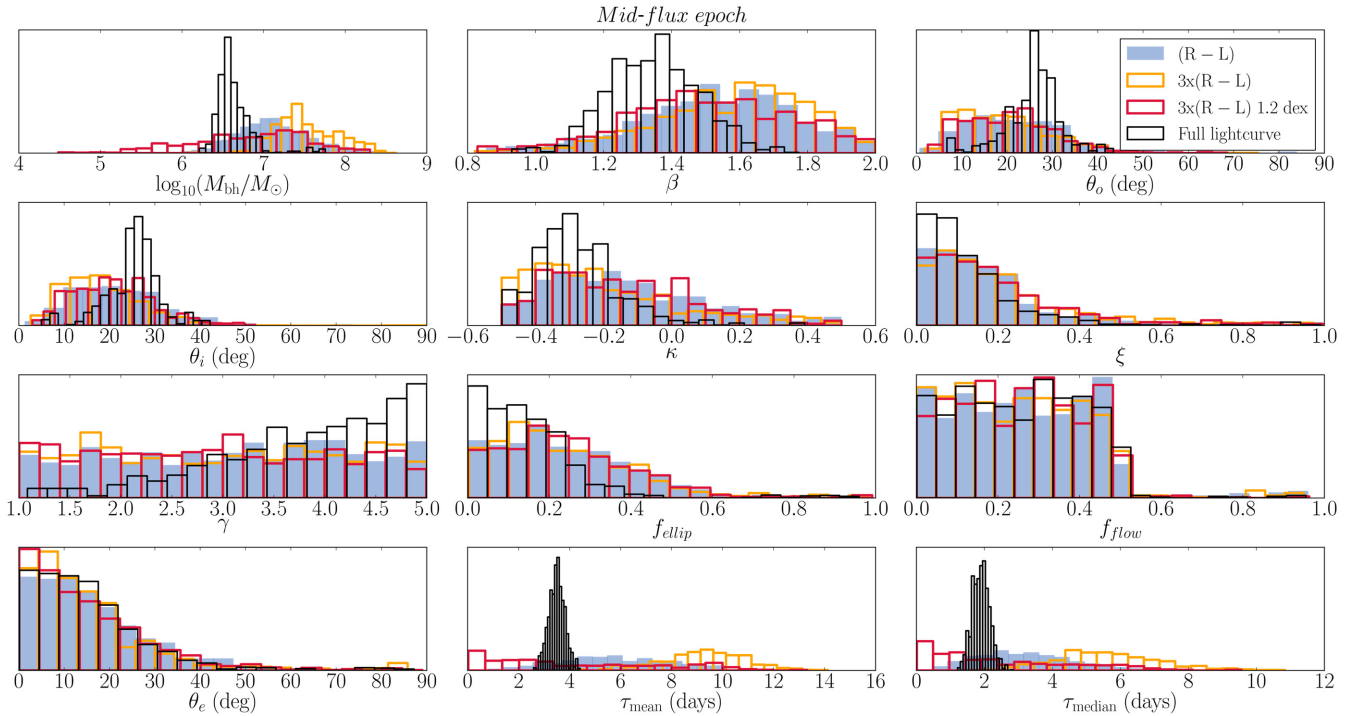


**Figure 9.** Posterior probability distributions for the BLR geometry and dynamics parameters determined using the mid-flux epoch. Default modelling of the full light curve without a Gaussian prior (Pancoast et al. 2018) is shown as the black solid line histogram. Blue: Gaussian prior on  $\tau_{\text{mean}}$  centred at the value found from the radius–luminosity relation and with  $\sigma_{\tau} = 0.2$  dex. Yellow: Gaussian prior on  $\tau_{\text{mean}}$  centred at  $3\times$  the time delay predicted by the  $R-L$  relation and with  $\sigma_{\tau} = 0.2$  dex. Red: Gaussian prior on  $\tau_{\text{mean}}$  centred at  $3\times$  the time delay predicted by the  $R-L$  relation and with  $\sigma_{\tau} = 1.2$  dex.

the three tests mentioned above provided equally good constraints on all the geometry and dynamics parameters. This means that even though the prior on the mean time delay changes in these tests, the model is able to extract the necessary information from the broad line profile. An exception to this is the black hole mass which is more sensitive to the time delay assumed. If one assumes a too narrow confidence range on  $\tau_{\text{mean}}$ , and by chance the  $R-L$  determined  $R_{\text{BLR}}$  is offset from the intrinsic  $M_{\text{BH}}$  value, this will result in a relatively narrow posterior distribution for the  $M_{\text{BH}}$  parameter but the mean value of the posterior distribution will be offset. The best approach to a more general application of this method is to set a wide prior that does not overly restrict the model, to take into account scenarios where the  $R-L$  determined  $R_{\text{BLR}}$  is uncertain or poorly constrained.

## 4 DISCUSSION

### 4.1 Constraining the geometry and dynamics of the BLR from single-epoch spectra

In this section we discuss the constraints that can be derived for the BLR geometry and dynamics parameters from modelling of single-epoch spectra, the effect of the signal-to-noise ratio and the particular features that may make Arp 151 a good test case.

In Table 3 we show the inferred values for the parameters and their respective 68 per cent confidence ranges obtained for each of our different tests. Each inferred parameter posterior probability distribution is determined by marginalizing over the remaining model parameters. The inferred parameter value is calculated from the median of the parameter posterior probability distribution. The distribution of the inferred parameters for each test can be visually

compared in Fig. 7. The black circles indicate the inferred values for the parameters and their respective 68 per cent confidence ranges. The shaded green vertical bars show the 68 per cent confidence range region for the full light-curve modelling inferred parameters (labelled as [1] in Fig. 7 and in Table 3). Both Fig. 7 and Table 3 will be used as reference for the discussion that follows in this section.

The BLR parameters can be divided into three groups, based on our analysis for the case of Arp 151: (1) parameters that are well constrained by single-epoch spectra; (2) parameters that depend on the epoch; (3) parameters that cannot be constrained by single-epoch spectra. We discuss each of these groups below.

#### 4.1.1 BLR parameters constrained by single-epoch spectra

Some of the inferred parameters show a consistent trend towards the full light-curve result, independently of the epoch chosen:  $\theta_o$ ,  $\theta_i$ ,  $\xi$ ,  $f_{\text{flow}}$ ,  $\theta_e$ .  $M_{\text{BH}}$  also does not depend strongly on the epoch. However, it is more closely connected with  $\tau_{\text{mean}}$ , and therefore can be biased if too stringent confidence ranges are imposed on the  $\tau_{\text{mean}}$  Gaussian prior, as in test number [9]. Fig. 10 shows the two-dimensional posterior probability distribution for  $M_{\text{BH}}$  and  $\tau_{\text{mean}}$  obtained for the mid-flux epoch to illustrate the dependence of the black hole mass on the mean time delay.

The three angles  $\theta_o$ ,  $\theta_i$ , and  $\theta_e$  are consistent within the 68 per cent confidence range with the inferred values from the full light-curve modelling. We find  $\theta_o = (9.3^{+19.6}_{-3.9}, 22.5^{+12.5}_{-10.7}, 12.5^{+12.3}_{-7.4})$  and  $\theta_i = (9.6^{+22.2}_{-3.7}, 22.5^{+10.6}_{-9.8}, 16.5^{+14.2}_{-7.8})$  for the low-flux, mid-flux, and high-flux epochs, respectively. While the median values seem to be underestimated for two of the epochs with respect to the value found from the full light-curve modelling ( $\theta_o = 26.4^{+3.9}_{-5.9}$  and  $\theta_i = 25.8^{+4.2}_{-5.7}$ ), the fact that all three values are consistent within

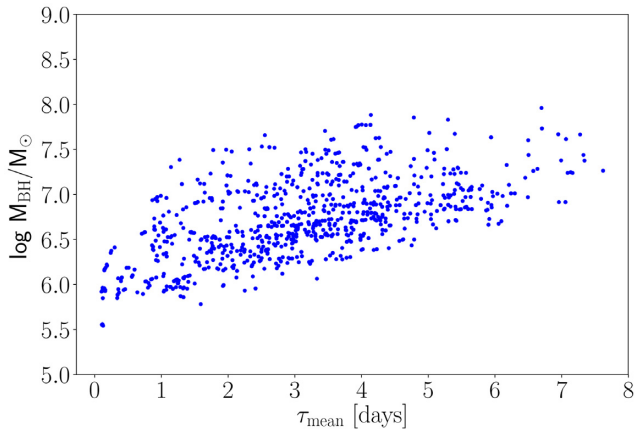


**Figure 10.** Figure illustrating the dependence between the black hole mass ( $M_{\text{BH}}$ ) and the mean time delay ( $\tau_{\text{mean}}$ ) for the mid-flux epoch of Arp 151. The values for the parameters were taken from the posterior probability distribution.

their 68 percent confidence region suggests that the perceived BLR angles do not vary strongly between epochs. The uncertainties associated with our inferred  $\theta_o$ ,  $\theta_i$  are only a factor of  $\sim 2$  higher than those from the full light-curve modelling. For  $\theta_e$  we find  $\theta_e = (27.3^{+43.2}_{-18.9}, 12.3^{+12.1}_{-8.3}, 17.9^{+27.8}_{-12.4})$  for the low-flux, mid-flux, and high-flux epochs, respectively. For the low-flux epoch,  $\theta_e$  is not well constrained by the data as can be seen from its broad 68 per cent confidence range. However,  $\theta_e$  for the mid-flux epoch is remarkably well constrained, and has a similar median value and similar uncertainties to the inferred full light curve  $\theta_e = 12.7^{+11.3}_{-8.6}$ .

In Fig. 11 we show the line profile shapes generated by the model, for a similar set of parameters as those inferred from the full light-curve modelling of Arp 151 and listed in column 2 of Table 3. This figure illustrates how the inclination angle and opening angle affect the line profile. The asymmetry between the blue and red peaks observed in the line profiles is due to a preference for the far side of the BLR to emit more ( $\kappa = -0.29$ ) combined with the inflowing gas orbits ( $f_{\text{ellip}} = 0.13$  and  $f_{\text{flow}} = 0.27$ ), which makes the blue-shifted emission more prominent than the redshifted emission. The effect of an almost opaque mid-plane ( $\xi = 0.09$ ) is mostly seen at low inclinations, due to the presence of the inflowing gas orbits. An example is the  $\theta_i = 0$  orbit with  $\theta_o = 15^\circ$ . For that case the mid-plane of the BLR is in the plane of the sky, which means that mostly only foreground gas is observed. As there is a strong component of inflowing gas orbits, by obscuring the background gas, it means that most of the blue-shifted component of the line-of-sight gas velocity is removed, skewing the line towards the red.

Similar to what was found in previous modelling of the full light curves (Pancoast et al. 2014b; Grier et al. 2017a; Pancoast et al. 2018), we find a correlation between the inclination angle and the opening angle. In Fig. 12 we show the two dimensional posterior distributions for Arp 151, showing the correlation between  $\theta_i$  and  $\theta_o$  colour coded as a function of black hole mass. As can be seen in Figs 11 and 12, an increase in inclination angle and opening angle, can be compensated by a decrease in black hole mass, so that small variations in these three parameters can produce various line profiles that are consistent. This results in several possible solutions for the angles that spread as a function of black hole mass. This dependence is mostly driven by the fact that larger black hole masses will increase the line of sight velocity of the gas and therefore increase the line profile width. The inclination affects the

line-of-sight velocity via a factor of  $\sin(\theta_i)$ , broadening the line profiles as the inclination increases.

There is also the question of why the opening angle and inclination angle are similar for Arp 151 (and in fact for most of the AGNs modelled via this technique – see Grier et al. 2017a for a discussion). In the simulations we show in Appendix A, the model is able to recover the real  $\theta_i$  and  $\theta_o$  for different setups, including  $\theta_i \sim \theta_o$ ,  $\theta_o > \theta_i$ , and  $\theta_o < \theta_i$ . This shows that the model does not drive the trend  $\theta_o \sim \theta_i$ . The fact that the angles found for real AGNs are similar is mostly due to the transition that occurs in the line profile when  $\theta_o \sim \theta_i$ . In a simplified way, a BLR with an inclination  $\theta_i$  and opening angle of  $\theta_o$  can be imagined as a collection of thin discs with inclinations between  $\theta_i - \theta_o$  and  $\theta_i + \theta_o$ . When  $\theta_o$  is of the order of, or higher than  $\theta_i$ , a significant fraction of orbits close to the plane of the sky will be included. These orbits have velocities close to the rest-frame velocity of the AGNs and therefore will transform the line profiles into ‘box-like’ profiles. For  $\theta_o \gg \theta_i$ , the line profiles will tend to have flatter tops. On the other hand, for  $\theta_o \ll \theta_i$ , the line profiles will tend to show double peaks. If the inclination is low, as one would expect for type 1 AGNs, a combination of low inclination and lower opening angles will result in the gas having a limited range in line of sight velocities creating line profiles that have more compact wings. Both the very boxy profiles and the compact wing profiles as generated by the model tend to not be a good representation of the observed line profiles for the sub-sample of AGNs analysed with the Pancoast et al. (2014a) code. In Fig. 13 we show different line profiles for the Arp 151 parameters to illustrate part of the  $\theta_i$  versus  $\theta_o$  parameter space for this AGN and the arguments outlined above.

As the line profiles for Arp 151 have a significant contribution from parameters that cause asymmetry, we produced line profiles using a simple structure for the BLR to isolate the effect of the inclination and opening angles. In Fig. 14 we show line profiles generated assuming that there was no inflow or outflow ( $f_{\text{ellip}} = 1$ ), a uniform distribution of particles ( $\gamma = 1$ ), a transparent mid-plane ( $\xi = 1$ ), and isotropic emission ( $\kappa = 0$ ). As can be seen from the figure, changing the inclination or opening angles make the line top flat or double-peaked and affect the width and shape of the tail of the emission line. The panel on the right shows that when the opening angle is lower than the inclination angle, and there are not significant asymmetries in the BLR, the profiles are difficult to distinguish, which means that for those cases the model may only be able to determine an upper limit for the opening angle.

The parameter  $f_{\text{flow}}$ , which describes the tendency of BLR particles to be in inflowing or outflowing orbits is also consistent ( $f_{\text{flow}} < 0.5$ ) for all the tests we carried out. A change in  $f_{\text{flow}} < 0.5$  to  $f_{\text{flow}} > 0.5$  causes a strong asymmetry in the spectral shape of the broad line. This is why this parameter is well determined from single-epoch data, as the information provided to the model comes from the line profile. In Fig. 15 we show examples of line profiles generated by our model for different combination of parameters, to illustrate possible configurations of the BLR and their influence on the line profile. Panels (a) and (b) of Fig. 15 show examples of line profiles where inflowing or outflowing orbits dominate (with  $f_{\text{flow}} = 0.27$  and  $f_{\text{flow}} = 0.73$ , respectively, and  $f_{\text{ellip}} = 0.13$ ). The signature of inflowing/outflowing orbits is asymmetric tails towards lower or higher wavelengths in the line profile. The tails are less pronounced if  $f_{\text{ellip}}$  is higher, which means that a smaller percentage of orbits are in inflowing or outflowing configurations. An example of this is shown in panel (c) of Fig. 15, which was generated assuming  $f_{\text{flow}} = 0.27$  and  $f_{\text{ellip}} = 0.9$ .

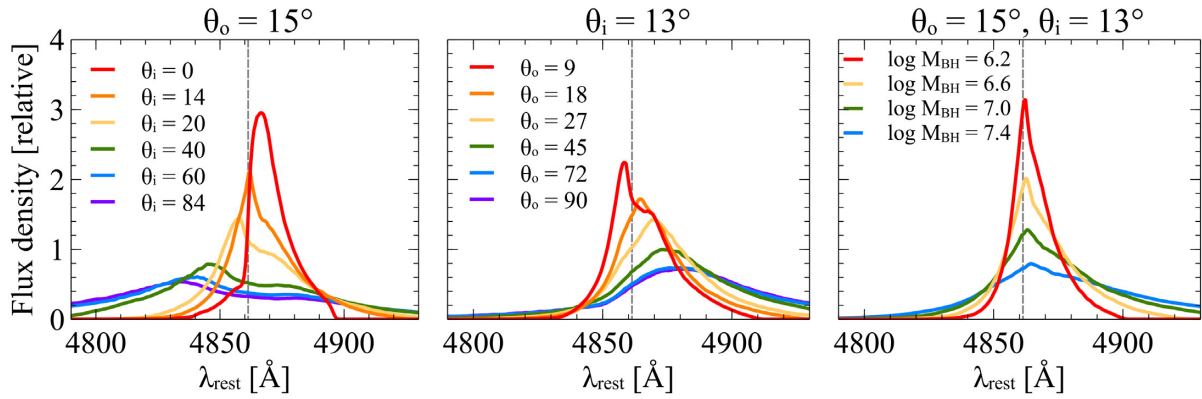


**Figure 11.** Simulated broad line profiles for different inclinations and opening angles for a case similar to Arp 151. The remaining parameters are set to the inferred values for Arp 151 quoted in column 2 of Table 3. The vertical dashed line indicates the central H $\beta$  rest-frame wavelength. The left-hand panel shows the effect of changing the inclination angle for a fixed opening angle of  $\theta_o = 15$  deg. The central panel shows the effect of changing the opening angle for a fixed inclination of  $\theta_i = 13$  deg. The right-hand panel shows the effect of changing the black hole mass for fixed inclination ( $\theta_i = 13$  deg) and opening angle ( $\theta_o = 15$  deg).

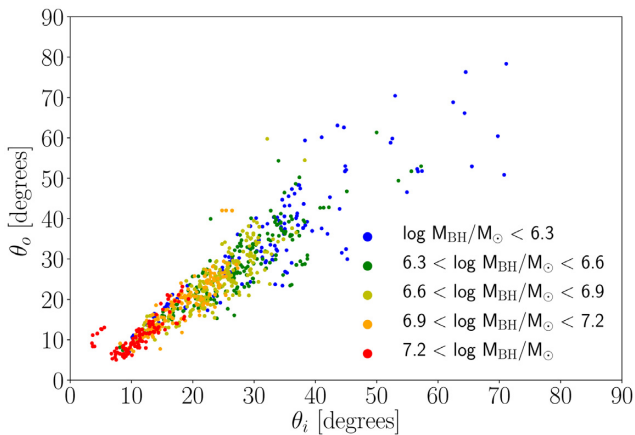


**Figure 12.** Figure illustrating the dependence between the inclination angle, opening angle, and black hole mass for Arp 151. The values for the parameters were taken from the posterior probability distribution. The coloured points represent different black hole mass bins.

We infer values of  $\xi = (0.19^{+0.51}_{-0.14}, 0.15^{+0.17}_{-0.09}, 0.17^{+0.34}_{-0.13})$  for the low-flux, mid-flux, and high-flux epochs, respectively. The median values of this parameter are similar to the result from the full light-curve modelling:  $\xi = 0.09^{+0.12}_{-0.06}$  with associated uncertainties that are a factor of  $\sim 1.5$ – $3.5$  times higher. For the low flux epoch, the values of  $\xi$  are still consistent within the uncertainties with the full light curve, however, the 68 per cent confidence region is very broad, which indicates that  $\xi$  is not significantly constrained for this epoch. The  $\xi$  parameter controls the BLR mid-plane transparency and is responsible for breaking the symmetry between the back and the front side of the BLR with respect to its mid-plane. This can be seen in Fig. 15. Panel (d) shows a case where  $\xi = 1$ , i.e. the BLR mid-plane is completely transparent, and it is fully outflowing ( $f_{\text{ellip}} = 0.0$ ). For this case, the line profile is close to symmetric for changes in  $\kappa$ . A similar line profile will be obtained for an inflowing BLR with anisotropic emission towards the ionizing source ( $\kappa < 0$ ) and an outflowing BLR with anisotropic emission away from the ionizing source ( $\kappa > 0$ ). A value of  $\xi \neq 1$  such as observed in Arp 151, will break the symmetry. This can be seen in panels (a)–(c) of

Fig. 15 that assume  $\xi = 0.09$ . Such behaviour could explain why  $\xi$  is constrained from single-epoch spectra.

Focusing on the three single epochs selected for Arp 151 (columns 3–5 in Table 3), we can see that the geometry and dynamics parameters mentioned above ( $\theta_o$ ,  $\theta_i$ ,  $\xi$ ,  $f_{\text{flow}}$ , and  $\theta_e$ ) can be determined with uncertainties that are comparable with those obtained using the full light curve, or up to a factor of 3.5 times higher, depending on the epoch. Such uncertainties are noteworthy considering that a single-epoch spectrum requires significantly less observing time than multi-epoch monitoring data.

We note that due to the probabilistic approach of our model, the parameter space is searched for all possible solutions (in terms of sets of parameters) that reproduce the line profile observed. Therefore, multiple solutions and their relative probabilities will be recorded and that information is part of the posterior probability distribution. The shape of the posterior distribution, that we characterize by the median value and 68 per cent confidence range, will contain the information about how well a parameter can be constrained from the data. In Fig. B4 in Appendix B we show the two dimensional posterior probability distributions, or corner plots for a selected set of our parameters for the mid-flux epoch.

#### 4.1.2 BLR parameters dependent on the epoch

The inferred values of some BLR parameters depend more strongly on the chosen epoch than others. The parameters that depend strongly on the epoch will show different distributions for each of the epochs but consistent distributions between mid-flux epoch [3] and the remaining tests. These are  $\beta$ ,  $\kappa$ , and  $f_{\text{ellip}}$ .

The parameter  $\beta$ , which controls the shape of the radial BLR cloud distribution, shows similar median values and uncertainties of up to a factor of 2 higher than the full light-curve result ( $\beta = 1.35^{+0.13}_{-0.13}$ ) for all the tests with the exception of the low-flux epoch. We find  $\beta = (1.75^{+0.15}_{-0.19}, 1.46^{+0.22}_{-0.22}, 1.53^{+0.12}_{-0.13})$  for the low-flux, mid-flux, and high-flux epochs, respectively. The low-flux epoch predicts a higher  $\beta$  than the full light-curve modelling. This may indicate that different portions of the BLR will react depending on a combination between the flux level and the prior continuum history. The line from the low-flux epoch may only be emitted from the regions closest to the black hole, which would result in a cloud distribution that decays more steeply with increasing radius. This is

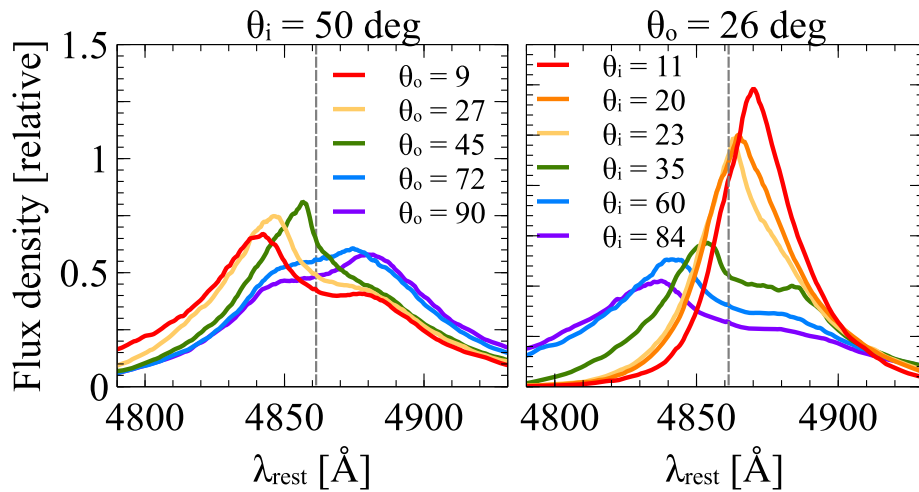


**Figure 13.** Simulated broad line profiles for different inclinations and opening angles for a case similar to Arp 151. The remaining parameters are set to the inferred values for Arp 151 quoted in column 2 of Table 3. The vertical dashed line indicates the central H  $\beta$  rest-frame wavelength. The left-hand panel shows the effect of changing the opening angle for a fixed inclination of  $\theta_i = 50$  deg, illustrating why high inclination angles are not considered a good fit of the observational data. The right-hand panel shows the effect of changing the inclination angle for a fixed opening angle ( $\theta_o = 26$  deg), corresponding to the inferred value of  $\theta_o$  from the full light-curve modelling of Arp 151. The right-hand panel illustrates the preferred inclination range of  $\theta_i \sim 10$ – $30$  deg found by the model.

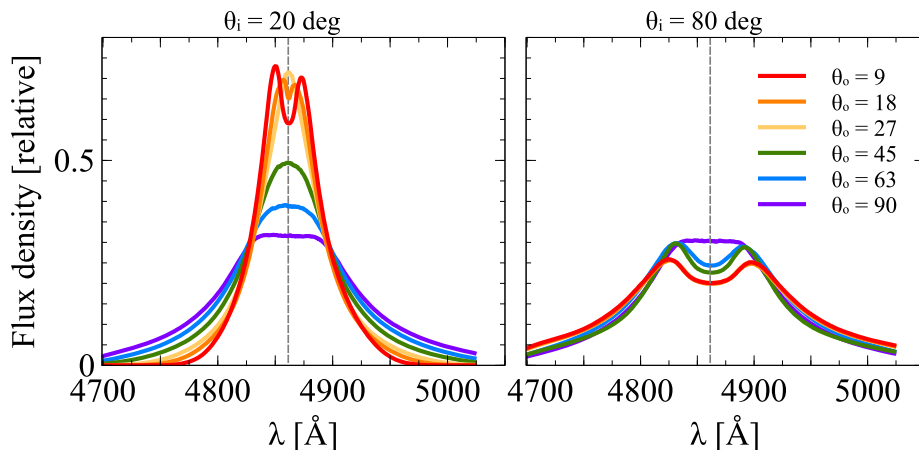


**Figure 14.** Simulated broad line profiles for different inclinations and opening angles. The vertical dashed line indicates the central H  $\beta$  rest-frame wavelength. To better illustrate the effect of changing the angles, the line profiles were generated assuming  $f_{\text{ellip}} = 1$ ,  $\gamma = 1$ ,  $\xi = 1$ , and  $\kappa = 0$ .

the so-called breathing effect: in low flux states it is expected that the BLR is smaller, more compact, and intrinsically more responsive (Netzer & Maoz 1990; Korista & Goad 2004; Cackett & Horne 2006). In this case, one would indeed expect a  $\beta$  value that is high, in line with the relatively high  $\beta$  value inferred from the modelling of the low-flux epoch compared to the other epochs. It may also depend on the previous continuum history and show effects of hysteresis: even if the flux is the same, the line profile may vary depending on whether the source was previously in a higher or lower flux state (e.g. Perry, van Groningen & Wanders 1994).

The  $\kappa$  parameter is related to a preferential BLR near-side or far-side emission relative to the ionizing source, as seen from the observer. All tests produce similar results for this parameter with the exception of the low and high-flux epochs, for which  $\kappa$  cannot be constrained. We find  $\kappa = (0.10^{+0.26}_{-0.37}, -0.18^{+0.23}_{-0.19}, 0.14^{+0.26}_{-0.34})$  for the low-flux, mid-flux, and high-flux epochs, respectively. The full light-curve result is  $\kappa = -0.29^{+0.11}_{-0.10}$ . The 68 percent confidence ranges for the low and high-flux epochs are consistent with both

negative and positive values, indicating that the ability to constrain  $\kappa$  may depend on the shape of the line profile which varies from epoch to epoch. In Fig. 15 we show an example of the effect of  $\kappa$  on the line profile. This parameter has a strong effect on the prominence of the tail of the line profile when inflowing or outflowing orbits are present, as can be seen in panels (a) and (b). However, the effect of  $\kappa$  is less noticeable when  $f_{\text{ellip}}$  is large, i.e. only a small fraction of orbits are in inflowing or outflowing configurations, as in panel (c) calculated with  $f_{\text{ellip}} = 0.9$ . It is difficult to distinguish the effect of small changes in  $f_{\text{ellip}}$  and  $\kappa$  in the line profile, for specific BLR configurations such as the one in Arp 151 (exemplified in Fig. 15). This explains why  $\kappa$  and  $f_{\text{ellip}}$  are difficult to constrain independently for every single epoch.

The parameter  $f_{\text{ellip}}$  shows a somewhat similar behaviour to  $\kappa$ , as mentioned above. It may depend on the epoch as the inferred parameters only marginally agree within the uncertainties. For the low-flux epoch  $f_{\text{ellip}}$  is mostly unconstrained. We find  $f_{\text{ellip}} = 0.40^{+0.37}_{-0.23}, 0.17^{+0.16}_{-0.11}, 0.35^{+0.20}_{-0.19}$  for the low-flux, mid-flux, and high-flux epochs,

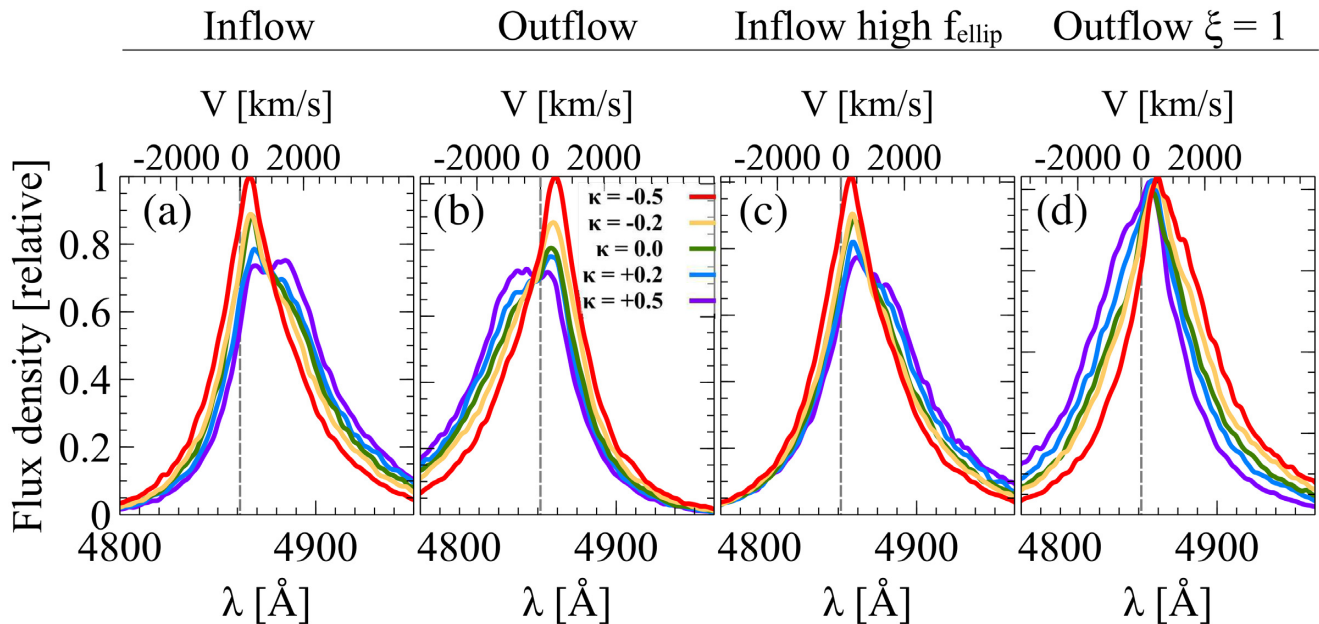


**Figure 15.** Model-generated line profiles as a function of geometry and dynamics parameters, illustrating how the BLR structure and kinematics affect the shape of the emission line in a single-epoch spectrum. The parameters  $f_{\text{flow}}$ ,  $f_{\text{ellip}}$ ,  $\kappa$ , and  $\xi$  are different in the four panels, otherwise the parameters used to generate the line profiles are similar to those inferred from the full light-curve result. The solid coloured lines represent the line profiles generated for different values of  $\kappa$ . Panels (a) and (b) show an example of the effect of inflowing and outflowing gas orbits, with  $f_{\text{flow}} = 0.27$  and  $f_{\text{flow}} = 0.73$ , respectively,  $f_{\text{ellip}} = 0.13$  and obscuration in the mid-plane of the BLR ( $\xi = 0.09$ ). Panel (c) shows a similar configuration to panel (a) with the only difference being a higher value of  $f_{\text{ellip}} = 0.9$ , i.e. less particles in unbound orbits. Panel (d) shows the effect of removing the obscuration in the mid-plane of the BLR ( $\xi = 1$ ), for a fully outflowing BLR ( $f_{\text{ellip}} = 0.0$ ). The vertical line indicates the rest frame of the  $\text{H}\beta$  emission line.

respectively. The full light-curve result is  $f_{\text{ellip}} = 0.13^{+0.11}_{-0.09}$ . The expression  $1 - f_{\text{ellip}}$  determines the fraction of particle orbits around the radial inflowing or outflowing escape velocity. It is interesting that  $f_{\text{flow}}$ , the parameter that determines if the  $1 - f_{\text{ellip}}$  particles are mostly close to inflowing or outflowing velocities, seems to be well determined and consistent for single epochs. If indeed  $f_{\text{ellip}}$  depends on the epoch, one interpretation is that the tendency for inflow or outflow does not change between epochs, but that the fraction of particles that can be in those inflows or outflows does change.

#### 4.1.3 Unconstrained BLR parameters

In our single-epoch spectra modelling,  $\gamma$ , the particle concentration, is almost completely unconstrained by the data for every test that we carried out. The parameter  $\gamma$  does not have a strong effect on the broad line spectral profile which is consistent with our findings of non-existent constraints on this parameter. From our tests we can conclude that single-epoch spectra may not be able to constrain  $\gamma$ , and is unlikely to be useful in BLR population studies.

#### 4.1.4 The effect of signal-to-noise ratio

The Arp 151 data we use in this work have high signal-to-noise ratio (S/N). The three epochs selected have  $S/N \sim 85$ –175 at the peak of the  $\text{H}\beta$  line. Fig. 4, right-hand panel, shows the S/N for each of the epochs after subtracting the continuum flux. The low-flux epoch that has the lowest S/N is also the epoch for which the posterior probability distribution functions for the parameters are broader, as can be seen from the 68 per cent confidence ranges in Fig. 7. This indicates that the parameters are more loosely constrained and

sometimes not constrained at all as shown in the previous sections. From the tests we did here, the mid-flux epoch is the one that provides inferred parameter values closest to the full light-curve modelling. However, the mid-flux epoch is not the one with the highest S/N. This suggests that successful modelling is not only a function of S/N but that it depends on other effects such as the line profile shape, discussed in the previous sections. Still, all the results of our tests have been obtained with relatively high quality spectra ( $S/N > 85$ ) when compared with all the single-epoch spectra available in the literature. This should be taken into consideration when selecting targets to extend the single epoch BLR modelling to a larger sample of AGNs.

#### 4.1.5 Arp 151 as a test case

Particular features of Arp 151 dataset make it a good test case. In addition to the high signal-to-noise mentioned above, the  $\text{H}\beta$  line profile in Arp 151 has the advantage of being reasonably well separated from other spectral features. In some AGNs the wings of the  $\text{H}\beta$  emission line are blended with other emission lines such as Fe II and He II, making it more difficult to separate broad and narrow emission features. This should be taken into account when modelling a larger sample of AGNs. In future work we will test the model's performance for AGNs in which the  $\text{H}\beta$  line profile is not so clearly isolated.

## 4.2 The effect of using monitoring data

In this section we discuss what would be the expected contribution to the model if timing information and spectral information (i.e.

a monitoring dataset) were to be used to constrain the model, as opposed to single-epoch spectra.

The first effect is the number of broad line spectral profiles that are used as input to the model. In our model we select single-epochs and therefore only one broad emission spectral profile is used as input. As a comparison, the input data used in the full light-curve modelling of Pancoast et al. (2018) contains 43 spectral profiles (a full spectral dataset). As can be seen from the results in this work, 43 spectra provide stronger constraints on the BLR parameters than a single spectrum. This is of course expected since the model tries to reproduce all the input spectra by searching the parameter space. It is also expected, as we see in our work, that not all of the parameters can be constrained from a single spectrum. The parameters that can be constrained using a single epoch spectrum will typically have larger uncertainties than when using the full monitoring data set.

The second effect is the timing information. Pancoast et al. (2014a) describe simulations using two different datasets to constrain the model: (1) flux light curves, comprised of the continuum flux light curve and the integrated  $H\beta$  line flux light curve; (2) continuum and integrated  $H\beta$  line flux light curves and a mean spectrum of the broad  $H\beta$  line. The first dataset contains only the light-curve information and no spectral information. They find that with this dataset, only the time delays and mean radius of the BLR are constrained by the model. All the remaining parameters are mostly unconstrained. This shows that the light curves mostly contain information on the time delays and size of the BLR. The second dataset simulated by Pancoast et al. (2014a) still contains the timing information from the light curves but adds the information contained in one spectrum which in the study by Pancoast et al. (2014a) is the mean spectrum. They find that the parameters inferred by the model are fully consistent with those determined from the modelling of the monitoring data, but with larger uncertainties. Since this second dataset contains the light curves and therefore timing information, they are able to constrain the time delays, radius of the BLR and black hole mass albeit with larger uncertainties than for the monitoring dataset case. Notably, the mean time delay and mean BLR radius have uncertainties that are ten times larger than those determined from modelling of the full monitoring dataset (light curves + spectra), indicating that the full spectral dataset has a major role in accurately constraining the time delays.

In our model we go one step beyond the second dataset referred to above. We exclude the light curves and therefore all the timing data completely. Our findings are similar to what Pancoast et al. (2014a) find using the second dataset: the parameters inferred are fully consistent with those determined when modelling the monitoring dataset but with larger uncertainties. The difference between using a single-epoch spectrum and the second dataset of Pancoast et al. (2014a) is the lack of timing information. As discussed above, the timing information determines the ability (or inability) of the model to constrain the time delays, radius of the BLR and to some extent the black hole mass. In this work we test the performance of the model when the timing information is replaced with information on the prior probability distribution of the mean time delay. Our findings are in agreement with what Pancoast et al. (2014a) found using the second dataset, in that our results are consistent with those from the monitoring dataset modelling but with larger uncertainties, with the exception of the  $\beta$  parameter which appears to change with the epoch. The other major difference is that without the light curves we are not able to independently determine the time delays and radius of the BLR. These parameters and the black hole mass will

be influenced by our selection of the prior probability distribution for the mean time delay.

### 4.3 Black hole mass

The black hole mass parameter is more sensitive to the prior constraint on  $\tau_{\text{mean}}$ , than other parameters, as can be seen from the first panel of Figs 7 and 10. Focusing on the result for the three different epochs (low-flux, mid-flux, and high-flux) we can see that the black hole mass obtained for each of the epochs is consistent with the one derived from the full light-curve modelling. The uncertainties, as expected, are larger than those obtained with the full light-curve modelling, of the order of 1 dex for each individual epoch. This uncertainty is similar to the inferred maximal statistical uncertainty estimated for mass determinations based on single-epoch spectra and black hole mass scaling relations (Vestergaard & Peterson 2006). We find  $\log_{10}(M_{\text{BH}}/M_{\odot}) = 7.20^{+0.56}_{-0.76}$ ,  $6.72^{+0.48}_{-0.42}$ ,  $6.89^{+0.51}_{-0.57}$  for the low-flux, mid-flux, and high-flux epochs, respectively. The full light-curve result is  $\log_{10}(M_{\text{BH}}/M_{\odot}) = 6.58^{+0.20}_{-0.12}$ . Our median black hole mass value is overestimated with respect to the full light-curve result. However, the analysis of the full light curves of Arp 151 from 2011 and 2015 provides higher inferred median  $M_{\text{BH}}$  values as well ( $\log(M_{\text{BH}}/M_{\odot}) = 6.93^{+0.33}_{-0.16}$  and  $\log(M_{\text{BH}}/M_{\odot}) = 6.92^{+0.50}_{-0.23}$ , respectively) (Pancoast et al. 2018). Our inferred median  $M_{\text{BH}}$  from single-epoch modelling is in better agreement with the 2011 and 2015 estimates. In general, when we assume a prior for the time delay, the inferred  $M_{\text{BH}}$  values are consistent, within the uncertainties, with the result of the full light-curve modelling. This is valid unless the mean value for that prior is significantly different (in our case by a factor of  $3\times$ ) from the real time delay and the prior assumes a narrow uncertainty. For future modelling of single-epoch spectra, the best approach is to use the  $R-L$  determined value for  $R_{\text{BLR}}$  but assume a conservative  $\sigma_{\tau}$  for the prior, so that the prior does not limit the parameter space search in case  $R_{\text{BLR}}$  is over- or underestimated. However, we highlight that the strength of our model is in determining the BLR geometry and dynamics parameters. Even with an overestimated mean value for the prior on  $\tau_{\text{mean}}$  the inferred parameters (with the exception of  $M_{\text{BH}}$ ) are remarkably consistent.

### 4.4 Future applications of the model

The fact that some of the parameters are being constrained by single epoch data is an encouraging result. It indicates that it is possible to extend BLR modelling to other AGNs for which only single epoch spectra and time lag estimates (possibly derived from the radius-luminosity relation) are available. In follow up papers we will utilize these new results to explore the potential of applying this modelling to a wider sample of AGNs, with and without monitoring data and spanning a wide range of redshifts. We will also use the same approach to model additional broad lines such as Mg II and C IV in particular for high redshift AGNs. Our ultimate goal is to constrain the typical BLR geometry and dynamical parameters for improved insight on the physics of the AGN central engine.

The BLR modelling in this work relies on an underlying physical prescription for the BLR. The free parameters in the model add flexibility to this prescription in that a variety of BLR configurations can be simulated by the model. However there is an intrinsic limitation to the physics that can be described by our model, and physical processes that are beyond the prescription assumed will not be captured by the model. Future applications of the model will be to include further physical processes that are known to be

important in the BLR, such as photoionization physics, radiation pressure, or winds. Comparing and implementing other underlying physical models for the BLR is also important, since there are currently several physical interpretations for the BLR that have been suggested to explain the current observational data (e.g. Goad, Korista & Ruff 2012; Elvis 2017).

## 5 CONCLUSIONS

The broad line region model of Pancoast et al. (2014a) has been successfully used to model monitoring data to determine the BLR geometry and dynamics of a small sample of local AGNs. However, due to the observational resources required, data from monitoring campaigns are only available for a small sub-sample of the known AGNs. In this work we modify the BLR model of Pancoast et al. (2014a) for application to single-epoch AGN spectra with the major modification being the addition of a prior probability distribution for the BLR size. We test our modified model to determine if it can be used to obtain meaningful constraints on the BLR parameters when single-epoch spectra (i.e. one single spectrum) are used.

We test our modified model on the AGN Arp 151, for which full light-curve broad line region modelling has been carried out by Pancoast et al. (2014b, 2018). The tests are performed by extracting single-epoch spectra from Arp 151's full light curve and analysing them independently. This setup tests for the first time the performance of the model when applied to data that does not contain timing information. We find that a large fraction of the BLR geometry and dynamics parameters inferred from single epoch spectra modelling are consistent within the uncertainties with the full light-curve modelling result. Our study identifies which BLR geometry and dynamics parameters are weakly dependent on the epoch, and therefore are the best candidates to be constrained by single-epoch spectra. Notably, these best candidate parameters: (the opening angle  $\theta_o$ , inclination angle  $\theta_i$ , the transparency of the BLR mid-plane  $\xi$ , the inflow or outflow orbits  $f_{\text{flow}}$  and the rotation angle between the circular and inflow/outflow orbits  $\theta_e$ ) can be determined from single-epoch spectra with uncertainties that are comparable with those obtained using the full light curve, or up to a factor of  $\sim 3.5$  times higher, depending on the epoch selected. Our tests indicate that BLR modelling using single-epoch spectra and an underlying physical model can provide constraints on the BLR structure. Considering the wealth of available single-epoch AGN observations, our approach can potentially be used to determine the overall AGN population trends in the geometry and dynamics of the BLR. We will further explore this opportunity in future work.

## ACKNOWLEDGEMENTS

The authors would like to thank the anonymous referee for a thorough review of the manuscript that improved the quality and clarity of the paper. The authors also thank Bradley Peterson for helpful discussions and comments on an early version of this work. The authors acknowledge financial support from the Independent Research Fund Denmark via grant no. DFF-4002-00275 (PI: Vestergaard). AP is supported by NASA through Einstein Postdoctoral Fellowship grant number PF5-160141 awarded by the Chandra X-ray Center, which is operated by the Smithsonian Astrophysical Observatory for NASA under contract NAS8-03060.

Research by AJB is supported by National Science Foundation grant AST-1412693.

## REFERENCES

- Barth A. J. et al., 2013, *ApJ*, 769, 128  
 Bentz M. C., Katz S., 2015, *PASP*, 127, 67  
 Bentz M. C. et al., 2009, *ApJ*, 705, 199  
 Bentz M. C. et al., 2010, *ApJ*, 720, L46  
 Bentz M. C. et al., 2013, *ApJ*, 767, 149  
 Blandford R. D., McKee C. F., 1982, *ApJ*, 255, 419  
 Brewer B. J., Pártay L. B., Csányi G., 2009, preprint (arXiv:0912.2380)  
 Brewer B. J., Pártay L. B., Csányi G., 2010, *Astrophysics Source Code Library*, record ascl:1010.029  
 Brewer B. J. et al., 2011, *ApJ*, 733, L33  
 Cackett E. M., Horne K., 2006, *MNRAS*, 365, 1180  
 Capriotti E., Foltz C., Byard P., 1980, *ApJ*, 241, 903  
 Collin S., Kawaguchi T., Peterson B. M., Vestergaard M., 2006, *A&A*, 456, 75  
 De Rosa G. et al., 2015, *ApJ*, 806, 128  
 Denney K. D. et al., 2010, *ApJ*, 721, 715  
 Du P. et al., 2014, *ApJ*, 782, 45  
 Du P. et al., 2018, *ApJ*, 856, 6  
 Elvis M., 2017, *ApJ*, 847, 56  
 Eracleous M., Halpern J. P., 1994, *ApJS*, 90, 1  
 Fabian A. C., 2012, *ARA&A*, 50, 455  
 Goad M. R., Korista K. T., Ruff A. J., 2012, *MNRAS*, 426, 3086  
 Grier C. J. et al., 2012, *ApJ*, 755, 60  
 Grier C. J. et al., 2013, *ApJ*, 764, 47  
 Grier C. J., Pancoast A., Barth A. J., Fausnaugh M. M., Brewer B. J., Treu T., Peterson B. M., 2017a, *ApJ*, 849, 146  
 Grier C. J. et al., 2017b, *ApJ*, 851, 21  
 Kaspi S., Smith P. S., Netzer H., Maoz D., Jannuzi B. T., Giveon U., 2000, *ApJ*, 533, 631  
 Kaspi S., Brandt W. N., Maoz D., Netzer H., Schneider D. P., Shemmer O., 2007, *ApJ*, 659, 997  
 Kollatschny W., Zetzl M., 2013, *A&A*, 549, A100  
 Korista K. T., Goad M. R., 2004, *ApJ*, 606, 749  
 Kormendy J., Ho L. C., 2013, *ARA&A*, 51, 511  
 Kozłowski S., 2017, *ApJS*, 228, 9  
 Kwan J., Carroll T. J., 1982, *ApJ*, 261, 25  
 Li Y.-R., Wang J.-M., Ho L. C., Du P., Bai J.-M., 2013, *ApJ*, 779, 110  
 Lira P. et al., 2018, *ApJ*, 865, 56  
 Lynden-Bell D., 1969, *Nature*, 223, 690  
 McLure R. J., Jarvis M. J., 2002, *MNRAS*, 337, 109  
 Netzer H., Maoz D., 1990, *ApJ*, 365, L5  
 Pancoast A., Brewer B. J., Treu T., 2011, *ApJ*, 730, 139  
 Pancoast A. et al., 2012, *ApJ*, 754, 49  
 Pancoast A., Brewer B. J., Treu T., 2014a, *MNRAS*, 445, 3055  
 Pancoast A., Brewer B. J., Treu T., Park D., Barth A. J., Bentz M. C., Woo J.-H., 2014b, *MNRAS*, 445, 3073  
 Pancoast A. et al., 2018, *ApJ*, 856, 108  
 Pei L. et al., 2017, *ApJ*, 837, 131  
 Perry J. J., van Groningen E., Wanders I., 1994, *MNRAS*, 271, 561  
 Peterson B. M., 1993, *PASP*, 105, 247  
 Peterson B. M., 1997, *An Introduction to Active Galactic Nuclei*, Cambridge Univ. Press, Cambridge  
 Peterson B. M., 2014, *Space Sci. Rev.*, 183, 253  
 Peterson B. M., Wandel A., 2000, *ApJ*, 540, L13  
 Peterson B. M. et al., 2004, *ApJ*, 613, 682  
 Raimundo S. I., Fabian A. C., 2009, *MNRAS*, 396, 1217  
 Rosenblatt E. I., Malkan M. A., Sargent W. L. W., Readhead A. C. S., 1994, *ApJS*, 93, 73

- Shankar F., Salucci P., Granato G. L., De Zotti G., Danese L., 2004, *MNRAS*, 354, 1020
- Shen Y. et al., 2011, *ApJS*, 194, 45
- Shen Y. et al., 2016, *ApJ*, 818, 30
- Skilling J., 2006, *Bayesian Anal.*, 1, 833
- Storchi-Bergmann T., Schimoia J. S., Peterson B. M., Elvis M., Denney K. D., Eracleous M., Nemmen R. S., 2017, *ApJ*, 835, 236
- Vestergaard M., 2002, *ApJ*, 571, 733
- Vestergaard M., 2004, *ApJ*, 601, 676
- Vestergaard M., Peterson B. M., 2006, *ApJ*, 641, 689
- Vestergaard M., Wilkes B. J., Barthel P. D., 2000, *ApJ*, 538, L103
- Walsh J. L. et al., 2009, *ApJS*, 185, 156
- Williams P. R. et al., 2018, *ApJ*, 866, 75
- Wills B. J., Browne I. W. A., 1986, *ApJ*, 302, 56
- Xiao M. et al., 2018, *ApJ*, 864, 109

## SUPPORTING INFORMATION

Supplementary data are available at *MNRAS* online.

**Appendix A.** Simulations.

**Appendix B.** Additional figures.

**Appendix C.** Choosing the temperature for the posterior distribution.

Please note: Oxford University Press is not responsible for the content or functionality of any supporting materials supplied by the authors. Any queries (other than missing material) should be directed to the corresponding author for the article.

This paper has been typeset from a  $\text{\TeX/L\AA\TeX}$  file prepared by the author.